Lawrence Berkeley National Laboratory

Title
An adaptable technique for comparative image assessment: Application to crosswell electromagnetic survey design for fluid monitoring

Permalink
https://escholarship.org/uc/item/9xp2375p

Journal
Geophysics, 86(3)

ISSN
0016-8033

Authors
Commer, Michael
Alumbaugh, David L
Wilt, Michael
et al.

Publication Date
2021-05-01

DOI
10.1190/geo2020-0430.1

Peer reviewed

An adaptable technique for comparative image assessment: application to crosswell electromagnetic survey design for fluid monitoring

Michael Commer[1]; David L. Alumbaugh[1], Michael Wilt[1], Abdullah Cihan[1]; Evan S. Um[1], Robin Petrusak[2], Jens T. Birkholzer[1]

Right Running Head: Target-adaptable image assessment

[1]Lawrence Berkeley National Laboratory, Energy Geosciences Division, Berkeley, California. E-mail: MCommer@lbl.gov; dalumbaugh@lbl.gov; mwilt@lbl.gov; acihan@lbl.gov; esum@lbl.gov; jtbirkholzer@lbl.gov.

[2]Advanced Resources International, Arlington, Virginia. E-mail: RPetrusak@adv-res.com.

An adaptable technique for comparative image assessment: application to crosswell electromagnetic survey design for fluid monitoring

(February 2, 2021)

Running head: **Target-adaptable image assessment**

ABSTRACT

Reservoir integrity stewardship accompanying carbon capture and sequestration considers reservoir fluid extraction and re-injection as a risk-mitigating method against reservoir overpressuring that could lead to caprock damage and ensuing CO_2-leakage. Crosswell electromagnetics offers a technically viable monitoring method with the spatial volume coverage necessary for reservoir-encompassing pressure management. However, a certain logistical dilemma for deep gas sequestration into saline and thus electrically conductive aquifers is that crosswell magnetic-field measurements underperform in the imaging of more resistive plume bodies, further exacerbated when vertical arrays intersect, as opposed to surround, plumes. Comparative synthetic-data plume imaging of such scenarios rates the information content of magnetic-field versus electric-field 3D crosswell layouts for reservoir and infrastructure conditions of a representative pilot site in a coastal area in Florida. The image quality of the resulting plume replications can be ranked numerically through a newly proposed semblance qualifier, appraising the model goodness of fit to a given reference. In contrast to common least-squares measures for goodness of fit, the semblance formulation employs classifying logistic function types, thus enabling a better distinction of predefined anomaly features.

INTRODUCTION

The U.S. Department of Energy formed the Brine Extraction and Storage Test (BEST) program to evaluate the technical feasibility of managing subsurface pressures associated with industrial-scale carbon capture and sequestration (CCS) (U.S. Department of Energy, 2016; Electric Power Research Institute, 2016; Okwen et al., 2017). The program provides field demonstration sites for testing pressure management strategies. One site is near the Lansing Smith Generating Plant near Panama City (Florida) mapped in Figure 1 together with existing well infrastructure. Freshwater instead of CO_2 will be injected to create subsurface pressure alterations to be managed. There are no plans to capture and store CO_2 at Plant Smith. Instead, investigative reservoir pressure management will involve active (pumped) and passive (driven by formation pressure equilibration) brine extraction from storage formations, concurrent with the water injection process (Birkholzer et al., 2012; González-Nicolás et al., 2019).

With the spotlight solely on pressure control, freshwater can be used as a proxy for injected supercritical CO_2 intended to remain in liquid phase. Being in a coastal area, the deep (around 1500 m) target reservoir is characterized by native brine; its low electrical resistivity will generate a large resistivity contrast to the added freshwater. The high fluid-induced resistivity difference in combination with the large reservoir depth and preexisting well infrastructure call for the crosswell electromagnetic (EM) method (e.g., Wilt et al., 1995a; 1995b; Wilkinson 2005; Marsala et al., 2008) as the method of choice for monitoring. Complementing sparse borehole-based pressure measurements, due to its larger volumetric coverage, crosswell EM will aid the critical subtask of spatiotemporal plume mapping. The method has shown potential in a variety of applications that involve

time-lapse monitoring of subsurface changes due to fluid flow (Alumbaugh and Morrison, 1995a; Wilt and Morea, 2004; Harris and Pethick, 2011; Hu et al., 2016) as well as for general reservoir reconnaissance (Hoversten et al., 2001, 2004; Shen et al., 2008; Wilt et al., 2008; Zhang et al., 2017). Here, we focus on the survey design based on simulations of the anticipated freshwater plume evolution.

Crosswell EM systems with well separations on the order of 100-300 m, as sketched in Figure 2, typically deploy inductively coupled antennas. Specifically, the systems use vertical magnetic dipole (VMD) transmitter coils for signal generation and induction coil receivers for magnetic field recording. For brevity, we will refer to this setup as VMD. The compactness of coils and the fact that casing effects can often be accounted for (e.g., Kirkendall et al. 1999, Cuevas and Pezzoli 2018), has given VMD systems greater attention both in the field as well as in theoretical studies (Spies, 1992; Alumbaugh and Morrison, 1995b; Liu et al., 1995; Spies and Habashy, 1995; Alumbaugh and Newman, 1997; Zhang et al., 1996; Zhang and Liu, 2000). However, it has been found that VMD systems face sensitivity limitations in the presence of typical CCS targets, that is, thin resistive anomalies within conductive regimes (Kong et al., 2009; Harris and Pethick, 2011; Grayver and Streich, 2014). On the contrary, vertical electric dipole (VED) systems are better suited for such targets (Grayver and Streich, 2014). This advantage comes at the expense of requiring open-hole or perforated fiberglass (or PVC) casing sections, because VED source signals inside conventional steel casing can generate measurable yet distorted fields (Kaufman and Wightman, 1993; Cuevas, 2018). Also, in contrast to the compactness of VMD coils, electric dipoles are less practical in-hole instruments as they may require antenna lengths on the order of meters or tens of meters to generate adequate source moments.

Our first objective is to provide more insights into the applicability of VMD systems

for CCS applications. To do so, we simulate 3D reservoir conditions for the BEST site, comparing the imaging capacity of VMD and VED data types and their combination. While we affirm findings about the better suitability of VED arrays for resistive CCS targets, a series of 3D trial inversions with standard VMD setups shows that ample resolution power can still exist for small resistors. However, as opposed to some oilfield scenarios with interwell targets, as exemplified in Figure 2, instrumented injection wells are more likely to cut through the inside of plumes, posing other challenges due to strong sensitivity variations near sensors.

Algorithmic and computational improvements have accompanied instrumental development in a way that 3D crosswell EM forward and inverse modeling can now routinely be used for survey-design decision-making (Tripp and Hohmann, 1993; van der Horst et al., 1999; Abubakar and van den Berg, 2000; Avdeev et al., 2002; Newman and Alumbaugh, 2002; Zhdanov and Yoshioka, 2003; Kim et al., 2004; Liang et al., 2010; Grayver and Streich, 2014; Zhang et al., 2017). Our second objective thus concerns the post-analysis of synthetic-data crosswell imaging experiments through rating their performance without solely depending on visual model inspection. Quantitative inverse-modeling solution rating is usually done via least-squares types of data-goodness-of-fit calculations. However, sequences of synthetic-data trial inversions for survey-design may yield equivalent data fits. Or, data fits may be difficult to compare if two solutions for the same target involve different data in terms of quantity, field types, noise assumptions, or survey geometry. Therefore, an additional secondary appraisal method relies on model goodness of fit.

Model goodness of fit in CCS contexts translates to quantifying property changes that unfold as subtle anomalies with respect to an initial, i.e., pre-injection, state. In this work, we employ a recently introduced formulation (Commer, 2020) that involves categorizing

logistic function types for calculating the model goodness of fit, as opposed to the data goodness of fit. Utilizing hydrogeophysical a priori information about temporal property evolution, we show that the new quantifier can capture subtle time-lapse model differences in inversion outcomes more accurately than traditional root-mean-square (RMS) formula types.

The philosophy behind the logistic-function concept is that in EM imaging, the priority is often to identify the nature of an anomaly. In other words, one wants to image a resistive or conductive anomaly, where the actual magnitude of resistivity (or conductivity) is secondary as long as certain anomaly thresholds are met. Such overshoot-forgiving threshold criteria are more amenable to classifying appraisers than they are to purely difference-based goodness-of-fit calculations.

In the next section, we first introduce the basic concepts of the new model-misfit formulation, which is referred to as semblance for brevity. Subsequent sections will compare the semblance against RMS qualifiers in order to appraise synthetic inversions with the goal of assessing the value of VMD and VED crosswell layouts for the reservoir conditions represented by the BEST site.

METHOD

The predominant way of assessing the performance of geophysical modeling is through misfit calculations, commonly involving the quadratic term (e.g., Menke, 2018)

$$\Phi = (\mathbf{p} - \mathbf{y})^T \mathbf{W}^T \mathbf{W} (\mathbf{p} - \mathbf{y}), \tag{1}$$

where the superscript T denotes transposition. When operating in data space, the functional returns the squared difference between a vector of size N of observed data $\mathbf{y}$ and its

corresponding data prediction $\mathbf{p} = F(\mathbf{m})$. Data predictions involve the forward-modeling operator F operating on a discretized earth model $\mathbf{m}$ with M components. Uncertainties are given through the weighting matrix $\mathbf{W}$. Weighing data misfit $p_i - y_i$ $(i = 1, \ldots, N)$ often involves a diagonal matrix $\mathbf{W}$ with entries of each measurement's inverse standard deviation $\frac{1}{\delta_i}$.

If used as an objective functional in inverse modeling, the minimizer of equation 1, which is the solution vector $\mathbf{m}$, is a best-fitting model of the actual subsurface property distribution, the latter referred to as $\tilde{\mathbf{m}}$ in the following. In imaging experiments with synthetic data, $\tilde{\mathbf{m}}$ refers to the true model, also to be called reference model, thus $\mathbf{y} = F(\tilde{\mathbf{m}})$. Note that, while opinions about this may deviate, for conciseness, we use the terms image and imaging interchangeably for, respectively, an inverse-modeling result $\mathbf{m}$ and the inversion process leading to it. We emphasize that equation 1 is written here solely as a starting point for the following derivation of metrics that assess the resemblance between an image $\mathbf{m}$ and its true state $\tilde{\mathbf{m}}$. These metrics are not intended to facilitate an inversion process.

A numerical performance rating for geophysical modeling is usually done via weighted least-squares metrics based on equation 1, calculating the data goodness of fit. However, sequences of synthetic-data inversions for survey design may yield model solutions with equivalent data fits. Therefore, to aid or replace visual image inspection, we base goodness-of-fit appraisal on discrepancies calculated between two models. Casting equation 1 into model space, $\mathbf{p} = \mathbf{m}$ and $\mathbf{y} = \tilde{\mathbf{m}}$. One can then deduce the weighted least-squares error

terms

$$\varepsilon(\mathbf{m}, \tilde{\mathbf{m}}) = \sqrt{\frac{1}{M} \sum_{i=1}^{M} \frac{(m_i - \tilde{m}_i)^2}{\delta_i^2}}, \tag{2}$$

$$\varepsilon^{log}(\mathbf{m}, \tilde{\mathbf{m}}) = \sqrt{\frac{1}{M} \sum_{i=1}^{M} \frac{\left(\log(m_i) - \log(\tilde{m}_i)\right)^2}{\delta_i^2}}. \tag{3}$$

These terms treat model discrepancies between a given true (reference) model $\tilde{\mathbf{m}}$ and its estimation (or image) $\mathbf{m}$ in a root-mean-square (RMS) sense. The logarithmic version addresses the fact that earth material properties like electrical resistivity or (hydraulic) permeability can exhibit large ranges, often over several orders of magnitude.

In model space, the terms δ_i^2 become model parameter variances. Their assessment involves the determination of covariances of the estimated parameters m_i $(i = 1, \ldots, M)$ (e.g., Carrera and Neuman, 1986). However, here we will use the weights $\frac{1}{\delta_i}$ in an entirely different way. Instead of calculating covariances, the δ_i will be made model-dependent in order to increase the sensitivity of error contributions in equations 2 and 3 to preselected features of interest. This adaptation is realized through casting δ_i into a categorizing function $\delta(m_i)$ with sigmoidal (S-shaped) function behavior. Before proceeding with this approach, we will first illustrate how sigmoidal functions can be used as a discriminator for model zones of interest.

Categorizing model features through sigmoidal functions

Sigmoidal functions (e.g., Newman 2016) essentially produce S-shaped curves to model a binary dependent variable with the output $f(x)=1$ for passing or $f(x)=0$ for failing preset criteria. Exemplified in Figure 3a for the logistic (a particular sigmoidal) function $f(x) = \frac{1}{1+e^{x_c-x}}$, such a criteria would be $f(x) \to 1$ for $x > x_c$ (passed) or $f(x) \to 0$ for $x < x_c$

(failed). The criteria can be adjusted by shifting the center x_c (here $x_c = 0$) along the x-axis. This logistic behavior can also be realized by a simple step-like (Heaviside) function. However, a gradual ascent from $f(x) = 0$ to $f(x) = 1$ as seen in Figure 3a allows for intermediate values $0 < f(x) < 1$, which might be useful if target criteria are partially met.

An example for a criteria defining an electrically resistive anomaly is illustrated in Figure 2 for the three parameter cells denoted by m_1, m_2, and m_3 and given the resistivity values of 10 Ωm, 50 Ωm, and 100 Ωm, respectively. Using the S function in Figure 3a with a threshold of $x_c = 50$ Ωm would produce $f(m_1) \approx 0$, $f(m_2) = 0.5$, and $f(m_3) \approx 1$, where $f(m_i) \geq 0.5$ might be used as the cutoff for labeling an element m_i as resistive.

Note that the exemplified bounding behavior of sigmoidal functions is somewhat similar to the concept of logarithmic upper and lower parameter bounds (Commer and Newman, 2008). Hence, it can be utilized to prevent overshooting error contributions in difference-based (RMS) types of errors as will be outlined in the following.

Fine-tuning RMS errors through sigmoidal weighting functions

Using S-shaped functions, a certain degree of adaptability to given target features can also be realized for the RMS error types, equations 2 and 3. The idea is to use the S-function behavior for capping error accumulations $m_i - \tilde{m}_i$ in order to avoid their domination. The capping is realized through making the weighting terms δ model-dependent. The dependency $\delta_i = \delta(m_i)$ involves a property limit, which is exemplified as $m^{lim} = 1.5$ in Figure 3b. Similar to x_c (Figure 3a), m^{lim} defines the center of the ascending (or descending) branch where the function changes from its minimum, δ_{min}, to its maximum, δ_{max}. In the following, δ is referred to simply as deviation.

The desired effect of a property-dependent deviation $\delta_i = \delta(m_i)$ is to attenuate over-shooting discrepancies $m_i - \tilde{m}_i$ when m_i meets a threshold defined by m^{lim}. Figure 3b exemplifies the two possible conditions. Consider the goal of delineating an electrically resistive anomaly. Its degree of resistivity above a certain threshold is assumed of minor importance. Note that we now switch to electrical conductivity, $\sigma = \frac{1}{\varrho}$, because all imaging results put forth below use this property. Imaging electrical conductivity $m_i = \sigma_i$, the function $\delta^+(m_i) \to \delta^{max}$ for (resistive) image elements $\sigma_i \ll \sigma^{lim} = 1.5 \frac{\text{S}}{\text{m}}$. A large devi-ation $\delta_i = \delta^{max}$ effectively dampens the corresponding contribution to the overall error ε (equation 2 or 3), thus keeping the focus on those discrepancies caused by more conductive elements $\sigma_i > \sigma^{lim}$. In other words, $\delta^+(\sigma_i)$ resembles a high-pass filter with the threshold σ^{lim} for errors caused by conductive elements, thus sensitizing ε to the delineation of a resistive anomaly defined by $\sigma_i < \sigma^{lim}$. Similarly, imaging a conductive target defined by $\sigma_i > \sigma^{lim}$ would employ the ascending function version, $\delta^-(m_i)$, which acts like a low-pass filter for misfits due to resistive elements. In practice, we implement this discriminating function behavior through the functions

$$\delta^+(m_i) = \delta^{max} - \frac{\delta^{max} - \delta^{min}}{1 + \exp\left(\frac{m^{lim} - m_i}{s}\right)}, \tag{4}$$

$$\delta^-(m_i) = \delta^{min} + \frac{\delta^{max} - \delta^{min}}{1 + \exp\left(\frac{m^{lim} - m_i}{s}\right)}, \tag{5}$$

where the steepness of the transition from δ^{min} to δ^{max} can be controlled by the scaling parameter $s > 0$. With $s \to 0$, $\delta(m_i)$ approaches a step function. Numerical examples will demonstrate that non-uniformly weighted RMS errors using equations 4 and 5 can quantify resemblance to the true anomaly in a more discerning way than uniformly weighted counterparts.

Quantifying model resemblance through sigmoidal functions

Replacing squared difference terms by sigmoidal function outputs takes the categorizing aspect a step further, which is the basis for a recently introduced model-comparing metric (Commer, 2020). We briefly outline the main concept here. The metric will be referred to as semblance S. It gears toward measuring the categorical resemblance between two models, as opposed to exactly quantifying discrepancies through difference-based metrics like equations 2 and 3.

To categorize anomalous model zones, we employ two discriminating function types. The first defines an anomaly in terms of its property range. Consequently, for a given image $\mathbf{m}$, the i-th contribution to the count of anomalous cells

$$N_a = N_a(\mathbf{m}, \tilde{\mathbf{m}}) = \sum_{i=1}^{M} f_i(m_i, a, b) \cdot f_i(\tilde{m}_i, a, b) \tag{6}$$

is non-zero only if (1) the preset criteria $a \leq m_i \leq b$ for an anomalous property range $[a, b]$ is met ($f_i(m_i, a, b) = 1$), and (2), it coincides with the reference, so $f_i(\tilde{m}_i, a, b) = 1$ for $a \leq \tilde{m}_i \leq b$. We refer to this categorizing function $f_i = f_i^{ab}$ as boundary condition. The function f_i^{ab} essentially has a square-like filter effect, which can be construed by concatenated ascending and descending branches of S functions or step functions (Commer, 2020).

The second anomaly-characterizing criteria describes relative (here, time-lapse) property changes that occur with respect to a given background model, $\mathbf{m}^0$. Equation 6 is thus augmented to

$$N_a(\mathbf{m}, \tilde{\mathbf{m}}) = \sum_{i=1}^{M} f_i^{ab}(m_i, a, b) \cdot f_i^{ab}(\tilde{m}_i, a, b) \cdot f_i^{\Delta}(m_i, \Delta^{lim}) \cdot f_i^{\Delta}(\tilde{m}_i, \Delta^{lim}). \tag{7}$$

The function product $f_i^{\Delta}(m_i, \Delta^{lim}) \cdot f_i^{\Delta}(\tilde{m}_i, \Delta^{lim})$ enforces a spatially coinciding (between

m and **m̃**) relative condition described by the threshold $\pm\Delta^{lim}$. The criteria for $f_i^{\Delta} = 1$ is met if a time-lapse change $\Delta = \frac{m_i - m_i^0}{m_i^0}$ relative to m_i^0 passes a limit set by $\pm\Delta^{lim}$. Note that throughout this work, both f^{ab} and f^{Δ} are truly binary classifiers, that is, $f_i = 0$ or $f_i = 1$ only. In other words, their S-shaped function branches as shown in Figure 3 become step functions.

Finally, the accumulation term for target-matching cell counts, equation 7, can be cast into the ratio

$$S = \frac{N_a(\mathbf{m}, \tilde{\mathbf{m}})}{N_a(\tilde{\mathbf{m}})} = \frac{\sum_{i=1}^{M} f_i^{ab}(m_i, a, b) \cdot f_i^{ab}(\tilde{m}_i, a, b) \cdot f_i^{\Delta}(m_i, \Delta^{lim}) \cdot f_i^{\Delta}(\tilde{m}_i, \Delta^{lim})}{\sum_{i=1}^{M} f_i^{ab}(\tilde{m}_i, a, b) \cdot f_i^{\Delta}(\tilde{m}_i, \Delta^{lim})} \cdot 100. \quad (8)$$

Values of S range from 0 % to 100 %, signifying the, respectively, lowest and highest semblance of an image **m** to the reference **m̃**. In principal, one can augment equation 8 by other classifiers f_i. Or, equation 8 can only involve f_i^{ab}, so that $N_a(\mathbf{m}, \tilde{\mathbf{m}})$ is given by equation 6.

Sigmoidal function types as objective functionals

Misfit formulas based on logistic functions, like the semblance S or the low-pass-filtering RMS weights, equations 4 and 5, can theoretically be weaved into minimizable objective functionals in order to constrain (joint) inverse modeling. However, we want to reiterate that in this work all misfit formulas are solely used for image post-processing, that is, they do not facilitate in any way the actual inverse modeling. Our trial inversions minimize an objective functional consisting only of a data misfit term similar to equation 1 and a regularizer imposing model-smoothness constraints. The underlying minimization algorithm uses a finite-difference (FD) forward modeling operator in conjunction with a standard non-linear-conjugate-gradient (NLCG) method (Commer and Newman, 2008).

ERROR-METRIC COMPARISON: 3D IMAGING OF CROSSWELL VMD DATA

Given the sensitivity differences that VMD and VED systems exhibit for resistive targets (Harris and Pethick, 2011; Grayver and Streich, 2014), an important question arising for CCS-specific survey design is whether the standard VMD system is adequate for delineating a resistive freshwater plume within the relatively conductive brine-saturated environment. Since deep CCS applications may involve similar resistivity contrasts, we dedicate the following series of 3D synthetic crosswell inversion studies to this question. Concurrent motivations are (1) to benchmark the proposed semblance measure against both unweighted and weighted RMS error types, and (2), to demonstrate how the new error terms based on sigmoidal functions may improve the quantitative image comparison to a known reference.

Sensitivity differences: Conductive versus resistive anomaly

We first tie in with the crosswell EM inversion studies of Alumbaugh and Morrison (1995b), because their findings about model resolution are relevant for the BEST survey design. The authors employed a 2D iterative Born imaging scheme within a cylindrically symmetric modeling context and explored, among many other aspects, what role the source frequency plays in model resolution. While higher frequencies lead to higher resolution, a limit is given by an increased signal attenuation, in addition to potential instrumental limits. Modifying one of their magnetic crosswell inversion setups for conductive targets, which is presented in figure 2 of Alumbaugh and Morrison (1995b), the anomalous target is now given by two 3D bodies of size 20 m × 20 m × 20 m as shown in Figure 4 (true geometry indicated by black contour lines). The 3D model space comprises a total of 29,172 FD cells as unknowns.

We pick the source frequency of 31 kHz, because at this frequency the vertical resolution becomes sufficient to separate the anomalous bodies, which are centered between two wells with 100 m separation. With magnetic coils spaced vertically at 10 m, both the transmitter (left well) and the receiver (right well) traverses have 21 activation points, resulting in 441 complex vertical magnetic field data points. Synthetic data generation follows the standard procedure of adding normally distributive random Gaussian noise to both real and imaginary components of the magnetic fields (measured in A/m). Noise magnitudes are based upon one percent of the data amplitude. For this study, we estimate an additional noise floor of 10^{-10} A/m from specifications of the instrument to be employed in the BEST survey, which depends largely on transmitter moment (Wilt et al., 1995a).

The two vertical sections in Figures 4a and 4b confirm that this VMD setup provides sufficient target reproduction, despite the relatively low target-to-background contrast of σ_a=0.02 $\frac{\text{S}}{\text{m}}$ to σ_0=0.01 $\frac{\text{S}}{\text{m}}$. Approaching the conditions at the BEST survey site, we repeat the same imaging test for a more resistive target, now with a target-to-background contrast of σ_a=0.005 $\frac{\text{S}}{\text{m}}$ to σ_0=0.01 $\frac{\text{S}}{\text{m}}$. The more blurred images in Figures 4c and 4d indicate the anticipated sensitivity loss.

Judging imaging performance in a quantitative way, Table 1 compares RMS imaging errors, equations 2 and 3, against the semblance alternative S. For a more straightforward comparison, all RMS (ε) errors are given as percentage decreases with respect to the inversion's starting model guess, the latter always using the background σ_0. Further, both uniformly weighted (ε, ε^{log}) and non-uniformly weighted (ε_δ, ε_δ^{log}) RMS errors are listed for comparison.

For the conductive target (Inversion 1, Figures 4a and 4b), the S-parameters a and b are

chosen such that the boundary condition holds as soon as a target cell conductivity results in $\sigma_a > \sigma_0$. Our choice of the relative condition states that a minimum conductivity increase of Δ^{lim}=20%, with respect to σ_0=0.01 $\frac{\text{S}}{\text{m}}$, qualifies as sufficiently anomalous. Similarly, for the resistive target (Inversion 2, Figures 4c and 4d), the boundary condition is met for all cells which are estimated as $\sigma_a < \sigma_0$, and the relative condition is met if σ_a has decreased by at least 20%. The parameters employed for the weighted RMS qualifiers attempt to mimic a similar threshold as given by $\Delta^{lim} = \pm 20\%$; therefore σ^{lim}=0.012 for Inversion 1 and σ^{lim}=0.008 for Inversion 2, which is a 20% deviation from the starting model value, σ_0.

Table 1 agrees with the visual perception that all error values appear to clearly distinguish between the higher-quality image of the conductive target (Inversion 1, Figures 4a and 4b) and the poorer image of the resistor (Inversion 2, Figures 4c and 4d). Compared to the unweighted RMS misfits, both weighted RMS %-improvements ε_δ and ε_δ^{log} and semblance percentages better highlight the image-quality discrepancies between both inversions.

We restate that the choice for the S-parameters, a, b, and Δ^{lim}, remains completely at the discretion of the user and will be dictated by specific a priori information about the target. The same holds for the parameters (function type and σ^{lim}) of the weighted RMS metric. For the case of Figure 4 (Inversions 1 and 2), where the anomalies contrast by a factor of two, we deemed the threshold of $\pm\Delta^{lim} = \pm 20\%$ and the corresponding boundaries for σ^{lim} as appropriate. The clear correlation between the difference in visually perceived image quality and the significant drop in S (from 82% to 48%) indicates a reasonable S-parameter choice for both inversions. Similarly pronounced reductions for both ε_δ and ε_δ^{log} echo this for their parameter choice.

Resolution differences: Resistors in a highly conductive regime

Alumbaugh and Morrison (1995b) presented a way of estimating the degree of spatial resolution for any combination of source frequency f, background conductivity σ_0, and transmitter-receiver separation $tx\text{-}rx$ (Figure 2). The estimate is given by the ratio $\frac{tx-rx}{\delta}$, where δ is the skin depth approximation, $\delta \approx 503\sqrt{\frac{1}{\sigma_0 f}}$ (in m). For the source frequency of f=31 kHz used above, one obtains $\frac{tx-rx}{\delta} \approx 3.5$ m, which can also be expressed alternatively in terms of the number of wavelengths, $\lambda_f = 2\pi\delta$, that fit into the distance $tx\text{-}rx$, amounting to $\frac{tx-rx}{\lambda_f} \approx 0.56$. Maintaining a similar ratio for the BEST site, where the background averages $\sigma_0 \approx 2 \frac{\text{S}}{\text{m}}$ in the reservoir layer, translates to a frequency $f \approx 150$ Hz.

Figure 5 summarizes the inversion outcome when using the source frequencies 500 Hz (Figures 5a and 5b) and 100 Hz (Figures 5c and 5d); for $\frac{tx-rx}{\delta}$, one obtains estimates of 6.3 ($\frac{tx-rx}{\lambda_f} \approx 1$) and 2.8 ($\frac{tx-rx}{\lambda_f} \approx 0.45$), respectively. Given these ratios, a degree of resolution similar to the cases in Figure 4 is expected, which is confirmed by the clearly delineated anomalies in Figure 5 as well as by the high semblance measures of $S \approx 87\%$ (for f=500 Hz) and $S \approx 75\%$ (for f=100 Hz). Note that by setting the parameter $b = \sigma_0 = 2 \frac{\text{S}}{\text{m}}$, the boundary condition becomes similarly lenient as before. Owing to the higher target-to-background contrast of $\sigma_a = 2 \frac{\text{S}}{\text{m}}$ to $\sigma_0 = 0.02 \frac{\text{S}}{\text{m}}$, we tightened the relative condition accordingly to $\Delta^{lim} = -30\%$. All ε-errors are consistent with the trend indicated by S, that is, the slightly lower resolution at f=100 Hz (Figures 5c and 5d) results in a poorer anomaly replication (Table 1, compare %-error improvement between Inversions 3 and 4).

The imaging experiments presented thus far demonstrate that despite the weaker resolving power of the vertical magnetic fields, compared to electric fields, in the presence of resistive anomalies, a 3D interwell anomaly can nevertheless be resolved using adequate

source frequencies.

Influence of target location: borehole-intersecting anomalies

The final inversion of this kind addresses the question how the target location may influence an inversion outcome. Economic constraints in CCS activities may dictate the instrumentation of injection wells, as opposed to drilling separate dedicated observation wells. This in turn will cause either source or receiver borehole arrays to traverse a plume body, as is also expected for the BEST survey. Such a scenario is modeled in Figures 6a–6d, showing the cross sections of the actual anomalies which are cylindrically shaped and centered around the transmitter well. Further adapting actual conditions of the BEST site, the receiver well is at a distance of 264 m from the injection well. To limit signal attenuation, we choose the source frequency of f=100 Hz, resulting in the images of Figures 6e–6h. The inversion achieves a vertical distinction of the anomalies and a fair match of the extent along the well plane (x-axis) (compare Figure 6a versus 6e). However, the horizontal disk size remains grossly underestimated (Figures 6b–6d versus 6f–6h), indicating that the VMD source placement inside the plume body lessens the sensitivity to these bodies, compared to interwell targets. Sensitivity maps shown below for the BEST site's actual configuration will provide further evidence for this issue. The low inversion performance manifests clearly in the low semblance value of S=10.6 (Table 1, Inversion 5) as well as in the marginal error improvement of the RMS-quantifiers.

We conclude this series of VMD imaging experiments with two takeaways. First, for each metric, the independent model inter-comparisons in Figures 4–6 span a percentage range given by the minimum and maximum errors in Table 1. Recall that all percentages are

error improvements with respect to the starting model. Hence, each metric's range reflects some general degree of sensitivity. The S-metric yields the largest range (10.6 – 82.1%), whereas ε (equation 2) exhibits the smallest range (5.6 – 30.9%), suggesting a generally more discerning ability of S.

Second, while of a rather academic nature, the imaging experiments point out the potential challenge that crosswell applications face when a resistive plume is centered at instrumented wells, rather than being located between wells. The following series of imaging trials specific to the BEST site will further investigate this issue.

CROSSWELL EM INVERSIONS FOR THE BEST SURVEY DESIGN

The BEST program's field demonstration site targets the deep (around 1500 m) Lower Tuscaloosa Massive Sand formation (e.g., Pair, 2017). Characterized by permeabilities up to 500 mD (milliDarcy), this formation is ideal for CO_2 storage. The target reservoir resides underneath confining layers. As indicated by the porosity log in Figure 7, relatively thin units within the injection interval are expected to facilitate generation of laterally extensive and thus easily detectable plumes of differential pressure and tracer content. Moreover, as also indicated by the resistivity log, one can expect a strong electrical conductivity contrast between the injected fluid and the ambient Tuscaloosa brine, the latter having 166,000 mg/L TDS (total dissolved solids of NaCl) on average (Electric Power Research Institute, 2016).

For hydrogeophysical site aspects, we refer to Appendix A which provides a brief description of the reservoir flow simulator employed. Also described is the petrophysical transformation procedure used for the generation of the models of electrical conductivity.

17

These models represent the electrical resistivity distribution at different plume stages. Figure 8 exemplifies a plume scenario after 18 months of injection together with the layered permeability model.

Crosswell survey configuration

For an areal map of the field site, see Figure 1. Existing infrastructure includes an injection well (TIW-2), a monitoring and extraction well (TEMW-A), and a repurposed monitoring and passive relief well (TIW-1). The well's rough location with respect to the anticipated plume extent became visible in Figure 8. The extraction well (TEMW-A) is steel-cased over the entire length, whereas both TIW-2 and TIW-1 will contain fiberglass sections over the region of interest. All three wells are perforated (screened) at the reservoir level to provide hydraulic contact. The fiberglass well sections will have the advantage of enabling an experimental VED deployment in addition to the conventional VMD array. Perforations create a galvanic contact and thus electric-field transmission between wellbore fluid and formation.

With well distances on the order of a few hundred meters, our VMD system that works via EM induction of currents into the formation has a general frequency operating range between 5 Hz and 1 kHz. Sufficient data quality for wells as far apart as 1 km could be achieved in this frequency range, also with one of the wells cased with standard carbon steel (Marsala et al., 2008, 2015). However, due to signal attenuation of the steel casing as well as nonlinear hysteretic effects, a steel well can only host the receiver, while the transmitter well must be either open or cased with a non-conductive liner such as fiberglass or PVC. Investigative forward modeling for the estimation of field-attenuation due to conductive

formation let us choose the frequencies of 60 Hz for VMD and 5 Hz for VED sources. Given the screening layout in combination with these frequencies, we neglect the potential influence of the casing materials on EM signal propagation in our numerical simulations. It is noteworthy though that in the frequency domain one can approximate the casing effect by means of a source signature correction with a complex factor (Wu and Habashy, 1994; Liu et al., 2008). Our presented studies do not employ such a correction. Further, regarding the specific VED layout, field planning that investigates signal differences between perforated and open wells is ongoing yet indicates rather minor differences in signal strengths; thus, VED layouts are also assumed to reside in open sections.

The well screening suggests two sets of transmitter-receiver array configurations. The first crosswell array deploys three galvanically coupled VED transmitters of length 10 m. These cover a 30 m long perforated section of the fiberglass-cased injection well (TIW-2). Their depths z=1490 m, z=1500 m, and z=1510 m traverse the injection interval. Signals are transmitted at 5 Hz frequency and received in well TIW-1. An array of 21 VED receivers that are spaced at 10 m covers a fiberglass section ranging from 1400 m to 1600 m in TIW-1, which is screened and thus open to the aquifer. This configuration, referred to as VED, is annotated as E_{Tx}(TIW-2) – E_{Rx}(TIW-1) in the site map (Figure 1) and comprises N_E=63 complex vertical electric-field data points. Since TEMW-A is fully steel-cased, it will be excluded from the VED set.

The second configuration is a VMD array with three transmitter-receiver well pairs, with the first given by H_{Tx}(TIW-2) – H_{Rx}(TEMW-A), the second by H_{Tx}(TIW-1) – H_{Rx}(TIW-2), and lastly H_{Tx}(TIW-1) – H_{Rx}(TEMW-A). Each well involves 21 dipoles over the depth range 1400 m to 1600 m, adding 441 complex vertical magnetic-field data points to a total of N_H=1323. Generally, (VMD) signal attenuation due to conventional steel casing becomes

significant for frequencies above a few tens of Hertz (Gao et al., 2008). Trial forward modeling revealed that the VMD source frequency of 60 Hz offers a compromise between our transmitter system's maximum power output and the (ideally high) induction level that can be reached in the conductive formation. Synthetic-data noise assumptions are the same as described above, with noise floor estimates of 10^{-10} A/m for the magnetic data. The VED system is currently being developed in-house; specifications suggest a value of 10^{-10} V/m for the electric fields.

The challenges that crosswell monitoring faces at the BEST survey site are twofold. First, the conductive regime causes a more rapid field attenuation, which limits the maximal achievable signal frequency, further impacting resolution as demonstrated above. Second, a relatively large ratio $\frac{tx-rx}{l_s}$ between well distance (tx-rx) and the vertical screen length l_s, the latter given by the traverse length of an instrumented borehole, can curb interwell sensitivity. In the context of ERT crosswell imaging, LaBrecque et al. (1996) recommend ratios below one. Referring to the inverse ratio $\frac{l_s}{tx-rx}$ as aperture, Alumbaugh and Morrison (1995b) also observed decreasing image resolution for apertures with $l_s < tx$-rx, here for a VMD crosswell pair with 10 kHz transmitter frequency. An ideal ratio is $\frac{tx-rx}{l_s} \approx 0.5$ (LaBrecque et al., 1996), which is fulfilled by the inversion tests of Figures 4 and 5.

Actual well distances at the BEST site are 264 m for the distance TIW-2 – TIW-1, 446 m for TIW-2 – TEMW-A, and 322 m for TIW-1 – TEMW-A (Figure 1). For our maximum screen length of l_s=200 m, one then obtains ratios of $\frac{tx-rx}{l_s}$=1.3, 2.2, and 1.6, respectively, indicating a generally less favorable geometry.

Estimating VMD and VED sensitivity

To obtain a more informative spatial sensitivity picture of the electric and magnetic crosswell configurations, we use a simple perturbation approach. Figure 9 presents maps of the term

$$D^{rel} = \frac{\sum_{i=1}^{i=N} |d_i^0 - d_i|}{\sum_{i=1}^{i=N} |d_i^0|}, \tag{9}$$

where d_i^0 and d_i denote unperturbed and perturbed data, respectively. Field amplitude (Figure 9b and 9e) and phase (Figure 9c and 9f) predictions are calculated for the true model, $\tilde{\mathbf{m}}$. Perturbed data d_i results from augmenting each cell parameter $\tilde{m}_i$ by 4%. Here, $\tilde{\mathbf{m}}$ is given by the plume model after 365 days of freshwater injection, because our survey-design objective assumes the plume target to be known. The plume is centered at the injector TIW-2, to be displayed in detail in imaging presentations below.

Equation 9 is a simple measure of summed data differences relative to the sum of unperturbed data, thus permitting a direct comparison between anomalous electric and magnetic field differences. Another approach would involve evaluation of the Jacobian, where sensitivity coefficients $\frac{d_i^0 - d_i}{\Delta \tilde{m}_i}$ from different field types would need to be made comparable to each other through appropriate scaling. Nonetheless, owing to the purpose of a crude sensitivity estimation, we refer to the term in equation 9 as sensitivity.

A first central observation in Figure 9 concerns the spatial distribution of areas where D^{rel} peaks. For the VMD component (Figures 9a–9c), maximal sensitivity occurs in the vicinity of TIW-1, upholding the observation that sensors that spatially coincide with the resistive plume center exhibit a loss of spatial sensitivity. Recall that this was also highlighted by the very localized anomaly reproduction in the horizontal image sections of Figures 6f–6h. Here, a sensitivity gap appears at TIW-2 where the resistive plume is centered. For the VED component (Figures 9d–9f), areas of heightened sensitivity coincide with the employed

well pair E_{Tx}(TIW-2) – E_{Rx}(TIW-1), as is expected for this field type.

A second observation concerns the sensitivity difference in magnitude between the two field types. As annotated in each sensitivity map, both the sensitivity maximum as well as its average are roughly an order of magnitude smaller for the magnetic field amplitude (compare Figures 9b and 9e). Phase sensitivities are generally small, with maximal differences between unperturbed and perturbed fields below one degree for the VMD setup (Figure 9c), and insignificant for the VED setup (Figure 9f).

Despite the greater volume coverage of the VMD configuration, this preliminary sensitivity information indicates an inferior recovery rate for this kind of off-centered and resistive target in a very conductive regime. The following site-specific imaging experiments will provide more evidence.

Inverting VMD and VED crosswell data

Initiating the inversion for the freshwater plume assumes the actual layered background as derived from the resistivity log of Figure 7 down to a depth of 1350 m, which is the top boundary of our inversion domain. Below, the conductivity is assumed constant at σ_0=3 $\frac{S}{m}$, which is an approximate average of the log over the vertical inversion domain. We terminated all inversions after 300 NLCG inversion iterations where the data misfit reduction became marginal. In order to match the fine scale of the flow simulation mesh, forward modeling for synthetic crosswell data generation involves a FD mesh with a horizontal mesh node distance of 5 m and a vertical distance of 2.5 m within the imaging volume. Given that the Lower Tuscaloosa reservoir properties such as permeability and porosity vary mostly along the vertical axis, our inversion mesh keeps the vertical spacing of 2.5 m, while using

a coarser spacing of 50 m along both horizontal axes. We found that this approach can alleviate the non-uniqueness problem of overparameterized inverse solutions to some degree. In the present case, the total number of model parameters would be M=1,653,750 if one would invert on the forward-modeling mesh, while the coarser imaging mesh decreases the problem size to M=200,000. Moreover, separation of forward- and inverse-modeling meshes makes synthetic-data inversions somewhat more realistic since real-world inhomogeneities near instruments are often likely to require a finer scale than allowable by numerical FD-meshing constraints. At last, note that yet another set of FD meshes is employed for the actual numerical solution of Maxwell's equations. Their mesh node distance varies with the source frequency as detailed in the description of our imaging method (Commer and Newman, 2008).

The first two inversions invert the VMD (data from two crosswell pairs, Figure 9a) and VED field setup (one crosswell pair, Figure 9d) separately, with the final outcomes shown in Figures 10b and 10c, respectively. As already indicated by the preceding inversion tests and sensitivity estimates, the resistive target remains poorly resolved by the magnetic field, whereas the VED setup leads to a much clearer picture. Nevertheless, some ability to illuminate the maximum horizontal plume dimension can be attributed to the VMD data. Ample resolving power along the well plane became evident through reproduction of both horizontal and vertical anomaly extent in the test case with borehole-intersecting targets (Figure 6). Hence, we surmise that the three well planes of the VMD setup also provide this kind of imaging ability, benefitting the (VMD+VED) joint inversion (Figure 10d). Particularly for the upper plume disk (around z=1,492 m), the joint inversion leads to a clearer reproduction of both geometry and resistivity magnitude.

Comparing the semblance percentages of the three inversion results, listed in Table 2

(column S), further supports the visually discerned image improvement resulting from the joint inversion. Here, the semblance term's criteria for detecting anomalously resistive cells are given by the parameters $[a, b]$=$[0, 1.11]$ (in $\frac{S}{m}$), and Δ^{lim}=-12% for a conductivity decrease deemed sufficiently anomalous. Starting at the obvious value S=0 for the whole-space initial model guess, S reflects a progressively better model reproduction, with S=13% for the VMD-data (Inversion 1), S=27.6% for VED (Inversion 2), and S=61% when combining both sets (Inversion 3).

For a fair comparison to S, we calculate the errors ε and ε^{log} over the whole inversion domain, and over a subset. The latter comprises all cells i of the actual model $\tilde{\mathbf{m}}$ which meet the boundary condition, so $\tilde{m}_i \in [a, b]$. Corresponding percentages (error decreases with respect to the initial model guess) are under the columns ε_{ab} and ε_{ab}^{log} in Table 2. The intent is to rule out error contributions not belonging to the anomaly.

The ε-type measures are consistent in signaling an insignificant model replication for all three inversions (1-3 in Table 2). Particularly for the VED and joint inversion, the single-digit percentage improvements with respect to the homogenous starting model defy the visually perceived image quality in Figures 10c and 10d. Several factors contribute to this discrepancy. First, all images are rather smooth, which is expected as the employed EM frequencies are too low to resolve the vertically fine pancake-structure of the anomaly. Further, the VMD inversion widely underestimates the resistive plume. In contrast, the VED image overestimates the central plume region (at z=1497.5 m), but underestimates most of its periphery. Combining VMD and VED data appears to yield the best match, however with some artifacts similar to the VMD image (compare Figures 10b and 10d). The corresponding semblance percentages in Table 2 echo these qualitative observations.

VMD and VED RMS errors as image quality criteria

The semblance metric's benefit is to provide a potentially more discerning model-goodness-of-fit criteria when potentially ambiguous data fits hinder the ranking of comparative synthetic imaging. Demonstrating RMS-error ambiguity, Figure 11 selectively plots amplitude and phase data for the VMD (Figures 11a and 11b) and VED (Figures 11c and 11d) component. The VMD data subset pertains to the well pair H_{Tx}(TIW-1) – H_{Rx}(TIW-2), with one chosen transmitter at z_{T_x}=1550 m (red symbol in subfigure of Figure 11a), whereas the VED subset pertains to E_{Tx}(TIW-2) – E_{Rx}(TIW-1) (z_{T_x}=1490 m). Corresponding RMS initial and final fitting errors are listed in Table 3 for standalone VMD and VED (Inversion No. 1 and 2) and joint (No. 3) inversions (columns denoted by "Initial[1]" and "Final[1]"). Using equation 2 for the reported RMS values, note that the model vectors $\mathbf{m}$ and $\tilde{\mathbf{m}}$ become data vectors for predictions and (synthetic) observations, respectively.

Both Figure 11 and Table 3 essentially point out that an error comparison based on data fits between standalone and joint inversion would remain ambiguous due to similar fits. For example, the joint inversion improves the final fit of the VED data portion only marginally (80.3%) over the standalone VED-data inversion (79.6%). The same holds for the errors calculated for the complete set (named VMD+VED in Table 3). One might wonder why these synthetic-data inversions do not lead to better fits in Figure 11. A perfect fit is ruled out by the aforementioned meshing discrepancy of 5 m versus 50 m for the horizontal node distance pertaining to the forward- and inverse-modeling meshes, respectively.

In view of the relatively high image quality obtained solely from the VED array, we will finish by appraising images of a hypothetical case, where only acquisition of the VED set would be possible.

Inverting VED data for different plume stages

Our inversion scheme employs a logarithmic conductivity parameter transformation with lower and upper conductivity parameter bounds (Commer and Newman, 2008), which can be made spatially variable. The final experiments employ such variable bounds in order to optimize the imaging capacity of the VED data through counteracting resistivity overshoots. Such overshoots, as observed for Inversion 2 (Figure 10c), can be spurred by too open bounds, which in this case were constant so that every imaging grid cell could vary over the same range, $[7.5 \times 10^{-3}, 3.1]$ $\frac{S}{m}$.

We let the plume geometry guide the spatially variable lower bounds. We first estimated a maximum plume extension based on extremal (hydraulic) permeability assumptions. The resulting maximal plume spreading was then approximated by a simple ellipsoid with the semiaxes (dx,dy,dz)=(500,500,120) m. Figures 12a and b show the actual plume simulated after 365 days of injection and the corresponding selection of lower bounds, respectively. With a minimum of 0.01 $\frac{S}{m}$ at the injection point (at TIW-2, z=1502.5 m), the lower bounds increase linearly outwards. Outside of the predefined ellipsoid, they remain constant at 2.9 $\frac{S}{m}$. The linear function is chosen such that for each cell parameter, the lower bounds always remain below their corresponding cell values $\tilde{m}_i$, as exemplified by the plume-cutting profile along y=0 (Figure 12c). This is to maintain an ample leeway for the inversion. Upper parameter bounds remain spatially constant at 3.1 $\frac{S}{m}$.

The assumptions underlying the variable lower parameter bounds are twofold. First, away from the injection point, there occurs more mixing of the brine's solutes with the spreading freshwater, leading to less resistive outer rings, which can also be seen in the horizontal sections of Figure 10a. Second, outside of the ellipsoidal volume of maximal

26

plume extension, no freshwater intrusion is expected. Hence, the permitted parameter changes in this region concern only adjustment of the background, which is realized by the tighter interval of [2.9,3.1] $\frac{S}{m}$.

Our final two inversions with this problem-specific parameter design have the goal of assessing whether a minimal crosswell setup as given by the VED component can discern between different plume stages. Figure 13 compares the actual plume with the corresponding image for the injection times 180 days (Figures 13a and 13b) and 365 days (Figures 13c and 13d). Qualitatively, the inversions track the plume's growth, although the full horizontal extent remains underestimated.

Lastly, we assess image qualities through the error measures in Table 2 (Inversions 4 and 5). While RMS error types remain rather imperceptive towards plume mapping, the significant semblance values of 38.1% and 46.4% support the qualitative observation that the VED layout offers some plume-tracking capacity. Compared to Inversion 2 (Figure 10c, S=27.6%), which used constant bounds, the higher S-value of Inversion 5 (Figure 13d, S=46.4%) numerically ascertains the improvements owing to the variable parameter bounds. The improvement can be attributed to a better suppression of the resistivity overshoots.

DISCUSSION

An ample variety of different survey geometries and models, in terms of their backgrounds and anomalous targets, is covered by the ten synthetic inversion demonstrations. All resulting images exhibit a good agreement between visually perceived quality and corresponding errors calculated using the new semblance measure S. This is a strong indicator that the semblance formulation might serve as a robust image evaluation tool. An automated ap-

praiser for model goodness of fit may be particularly useful for ranking a large number of images with comparable data fits. Moreover, a solely visual 3D check of many images may not always be easily done in the presence of complex or subtle anomaly structures.

Using the semblance metric without visual cross check will require further amendments in order to handle excessive imaging artifacts. Consider for example the resistive interwell anomaly in Figure 2 and an extreme image, albeit improbable, where every cell parameter assumed $m_i \geq 50\ \Omega$m. With semblance parameters $[a,b] = [50, \infty]\ \Omega$m defining the resistor, one would have $f_i(m_i, a, b) = 1$ for all i $(i = 1, \ldots, M)$. The image semblance would amount to $S=100$ %, because of $f_i(m_i, a, b) \cdot f_i(\tilde{m}_i, a, b) = 1$ (equation 6) for target cells and zero otherwise (due to $f_i(\tilde{m}_i, a, b) = 0$).

The example illustrates an indifference of the semblance metric to such artifacts, whereas RMS error types would show an effect. Paying this price for better target sensitivity may occur for other non-difference types of metrics. Another such metric is often used for structural model inter-comparison in joint imaging and uses the cross-gradient concept (Gallardo and Meju, 2003). Similar to the above example, a region outside the target zone that is homogenous in the reference model $\tilde{\mathbf{m}}$ but exhibits artifacts in form of property gradients in an image $\mathbf{m}$ would also produce vanishing and thus indifferent cross-gradient contributions, $\nabla \tilde{\mathbf{m}} \times \nabla \mathbf{m} = 0$.

In our case, a possible remedy would change the indifference of $f_i(\tilde{m}_i, a, b) = 0$ in the presence of non-target imaging artifacts to a penalizing behavior $f_i(m_i, a, b) \cdot f_i(\tilde{m}_i, a, b) < 0$. Such penalty terms could then offset positive contributions so that a very small S or even $S \leq 0$ becomes an indicator for excessive artifacts.

Our imaging studies did not produce strong artifacts. This perhaps more common case

reveals that RMS-based errors are more susceptible to spurious error contributions owing to smooth images. Similarly, overestimated as well as underestimated target properties, even if anomalous trends are predicted correctly, can obscure an overall upgrade of one image over another. Here we proposed a method for alleviating the latter issue by means of proxy deviations, which effectively dampen RMS error contributions from image elements which correct but overshooting trends. While partially successful, image smoothness remains problematic for all difference-based metrics.

CONCLUSIONS

Our EM inversion experiments for the BEST pilot site indicate that a plume-tracking capability can be achieved with crosswell arrays that involve a reasonably low logistical effort. Given the resistivity and geometry of the target, both sensitivity estimations and trial inversions suggest that the VMD component will be inferior to the VED setup. Nevertheless, joining both data sets has shown merit by matching the actual plume extension closer.

Regarding survey-planning considerations, the imaging results suggest to strive for maximizing the data's information content by gathering both the VMD and VED data in the field. However, if unforeseen economical constraints or instrumental failures would impede an exhaustive data collection, the imaging quality achieved by the standalone VED inversions indicates that time-lapse plume-mapping information can still be achieved. While casing-material effects were neglected, it is self-understanding that a more refined survey planning will need to include such effects. Other effects to consider are linked to anisotropic intrinsic permeability in the reservoir zone, causing potential electrical anisotropy.

A number of future CCS sites will likely be situated over subsurface reservoirs where

CO_2-injection produces an electrical resistor within a conductive (brine-saturated) regime. Owing to their superior sensitivity for such targets, we recommend to prioritize VED systems in the survey design. Notwithstanding, using only one data type makes inversion results more vulnerable to its shortcomings, here manifesting as resistivity overshoots combined with underestimated plume disk sizes in the VED images. Estimating conductivity parameter boundaries based on the modeling of extremal flow conditions, we were able to alleviate this issue to some degree. The boundary constraints effectively couple some of the underlying physics of the fluid injection to the geophysical inversion. Although being a simplistic approach, for survey design with a fluid-monitoring objective it may be preferable over an otherwise decoupled inversion.

ACKNOWLEDGMENTS

Reagan for providing the basis for Figure 8.

APPENDIX A

RESERVOIR FLOW MODEL

We employ a numerical flow simulator which solves combinations of the coupled continuity equation, advection-diffusion equation, and Darcy equation. It has been applied in earlier CCS contexts (Agartan et al., 2017; Siirila-Woodburn et al., 2017). Properties of the fluid mixture (compressibility, density, and viscosity) are computed as a function of salt mass fraction, pressure and temperature, using the correlations developed by Phillips et al. (1981) and Spivey et al. (2004). These correlations cover a wide range of salinity (up to 5.7 mole/kg), temperatures (0° to 275° C), and pressures (up to 200 MPa) and thus are suitable for the depth range of the Tuscaloosa formation. Static depth-dependent temperature variation is accounted for, while we neglect dynamic heat flow. The coupled non-linear partial differential equations are discretized by the finite-volume method and solved through the Newton-Raphson method. At each Newton-Raphson iteration, the linearized system of equations is solved by a preconditioned restarted Generalized-Minimum-Residual algorithm.

The simulated injection scenario considers a constant rate of 1090 $\frac{\text{m}^3}{\text{day}}$ ($\approx$200 $\frac{\text{gal}}{\text{min}}$) of low-salinity water characterized by 1,000 to 1,200 mg/L TDS. The target reservoir is given by isolated sandstone layers of the Lower Tuscaloosa Massive Sand formation, where actual injection will occurs between 1,487 to 1,536 m (4,880 and 5,038 feet), as indicated in the geological section of Figure 7. In this zone, permeability ranges from 0.5 mD to over 1,000 mD and porosity ranges from 10% to over 50%. Simulating an injection that lasts 18 months results in a plume model as shown by Figure 8. Freshwater is characterized by

low salinity (blue), in contrast to the saline native brine (red). Also shown is the vertical permeability profile for the reservoir zone.

Petrophysical flow model transformation

The reservoir flow model encompasses the Lower Tuscaloosa and Lower Cretaceous sediments at the site (Figure 7). Reservoir properties that have the most influence on electrical rock properties are (fractional) porosity Φ, solute concentration C of the connate water, and temperature T. The Tuscaloosa sandstones in the area of interest are friable, weakly cemented sandstones, suggesting that bulk ionic migration through the pores of the rock is the main contributor to the rock's electrical resistivity. Consequently, electrical conduction along the surface of the grains of the rock is negligible, so the law of Archie (1942) in the simple form

$$\varrho = \varrho_f F; \quad F = 0.62\Phi^{-2.15} \tag{A-1}$$

is applicable. Fluid electrical resistivity (in Ωm) is quantified by ϱ_f. The specific relation for the formation factor F is based on empirically derived measurements on Gulf-Coast sandstones (Winsauer et al., 2017). Poroelastic deformation is neglected, that is, porosity is assumed constant during the fluid-injection process. Hence, the main driving reservoir property that controls the changing EM geophysical footprint during injection is $\varrho_f = \varrho_f(C, T)$.

Reservoir modeling delivers a 3D distribution of solute concentration (Figure 8). Freshwater injection causes a gradual dilution of the reservoir's brine, where salinity is measured as the fractional concentration C of NaCl. Using tabulated $C, T, \varrho_f(C, T)$ data of NaCl solutions (Schlumberger, 2009), where we assume a constant reservoir temperature of

$T = 35°$ C, together with porosity logs (Figure 7), we obtain the distribution of ϱ via the Winsauer model (equation A-1). Our EM modeling implementation inverts for electrical conductivity, $\sigma = \frac{1}{\varrho}$. Hence, all shown images and misfit calculations involve models of σ.

REFERENCES

Abubakar, A., and P. M. van den Berg, 2000, Three-dimensional inverse scattering applied to cross-well induction sensors: IEEE Transactions on Geoscience and Remote Sensing, **38**, 1669–1681.

Agartan, E., A. Cihan, T. H. Illangasekare, Q. Zhou, and J. T. Birkholzer, 2017, Mixing and trapping of dissolved co2 in deep geologic formations with shale layers: Advances in Water Resources, **105**, 67–81.

Alumbaugh, D. L., and H. F. Morrison, 1995a, Monitoring subsurface changes over time with cross-well electromagnetic tomography: Geophysical Prospecting, **43**, 873–902.

———, 1995b, Theoretical and practical considerations for crosswell electromagnetic tomography using a cylindrical geometry: Geophysics, **60**, 846–870.

Alumbaugh, D. L., and G. A. Newman, 1997, Three-dimensional massively parallel electromagnetic inversion - II. Analysis of a crosswell electromagnetic experiment: Geophysical Journal International, **128**, 355–363.

Archie, G. E., 1942, The electrical resistivity log as an aid in determining some reservoir characteristics: Transactions of the American Institute of Mining, Metallurgical, and Petroleum Engineering, **146**, 54–62.

Avdeev, D. B., A. V. Kuvshinov, O. V. Pankratov, and G. A. Newman, 2002, Three-dimensional induction logging problems,Part I: An integral equation solution and model comparisons: Geophysics, **67**, 413–426.

Birkholzer, J. T., A. Cihan, and Q. Zhou, 2012, Impact-driven pressure management via targeted brine extraction? conceptual studies of CO2 storage in saline formations: International Journal of Greenhouse Gas Control, **7**, 168–180.

Carrera, J., and S. P. Neuman, 1986, Estimation of aquifer parameters under transient and

steady state conditions: 1. Maximum likelihood method incorporating prior information: Water Resources Research, **22**, 199–210.

Commer, M., 2020, A semblance measure for model comparison: Geophysical Journal International, **224**, 1301–1313.

Commer, M., and G. A. Newman, 2008, New advances in three-dimensional controlled-source electromagnetic inversion: Geophysical Journal International, **172**, 513–535.

Cuevas, N., 2018, Analytical solutions of em fields due to a dipolar source inside an infinite casing: Geophysics, **79**, E231–E241.

Cuevas, N., and M. Pezzoli, 2018, On the effect of the metal casing in surface-borehole electromagnetic methods: Geophysics, **83**, E173–E187.

Electric Power Research Institute, 2016, Phase II field demonstration at Plant Smith Generating Station: Assessment of opportunities for optimal reservoir pressure control, plume management and produced-water strategies: https://www.netl.doe.gov/sites/default/files/netl-file/20180410_0930B_Presentation_FE0026140_EPRI.pdf, accessed 10 June 2020.

Gallardo, L. A., and M. A. Meju, 2003, Characterization of heterogeneous near-surface materials by joint 2D inversion of dc resistivity and seismic data: Geophysical Research Letters, **30**, 1658.

Gao, G., D. L. Alumbaugh, P. Zhang, H. Zhang, C. Levesque, R. Rosthal, J. Liu, A. Abubakar, and T. Habashy, 2008, Practical implications of nonlinear inversion for cross-well electromagnetic data collected in cased-wells: 78th Annual International Meeting, SEG, Expanded Abstracts, 299–303.

González-Nicolás, A., A. Cihan, R. Petrusak, Q. Zhou, R. Trautz, D. Riestenberg, M. Godec, and J. T. Birkholzer, 2019, Pressure management via brine extraction in geological CO2

storage: adaptive optimization strategies under poorly characterized reservoir conditions: International Journal of Greenhouse Gas Control, **83**, 176–185.

Grayver, A. V., and O. Streich, R. Ritter, 2014, 3D inversion and resolution analysis of land-based CSEM data from the Ketzin CO2 storage formation: Geophysics, **79**, E101–E114.

Harris, B., and A. Pethick, 2011, Comparison of a vertical electric and a vertical magnetic source for cross well CSEM monitoring of CO2 injection: 81st Annual International Meeting, SEG, Expanded Abstracts, 1892–1896.

Hoversten, G. M., P. Milligan, J. Byun, J. Washbourne, L. C. Knauer, and P. Harness, 2004, Crosswell electromagnetic and seismic imaging: an examination of coincident surveys at a steam flood project: Geophysics, **69**, 406–414.

Hoversten, G. M., G. A. Newman, H. F. Morrison, E. Gasperikova, and J.-I. Berg, 2001, Reservoir characterization using crosswell electromagnetic inversion: A feasibility study for the Snorre field, North Sea: Geophysics, **66**, 1177–1189.

Hu, Y., Z. Yu, W. Zhang, Q. Sun, and Q. H. Liu, 2016, Dynamic fluid flow and electromagnetic fields for subsurface sensing: IEEE Journal on Multiscale and Multiphysics Computational Techniques, **1**, 14–25.

Kaufman, A. A., and W. E. Wightman, 1993, A transmission-line model for electrical logging through casing: Geophysics, **58**, 1739–1747.

Kim, H. J., Y. Song, K. H. Lee, and M. J. Wilt, 2004, Efficient crosswell EM Tomography using localized nonlinear approximation: Exploration Geophysics, **35**, 51–55.

Kirkendall, B., P. Harben, and P. Lewis, 1999, Advances in crosswell electromagnetics: steel cased boreholes: 69th Annual International Meeting, SEG, Expanded Abstracts, 323–326.

Kong, H. J., F. Roth, P. A. Olsen, and S. O. Stalheim, 2009, Casing effects in the sea-to-

borehole electromagnetic method: Geophysics, **74**, F77–F87.

LaBrecque, D. J., A. L. Ramirez, W. D. Daily, A. M. Binley, and S. A. Schima, 1996, ERT monitoring of environmental remediation processes: Measurement Science and Technology, **7**, 375–383.

Liang, L., A. Abubakar, and T. Habashy, 2010, Three-dimensional fluid-flow constrained crosswell electromagnetic inversion: 80th Annual International Meeting, SEG, Expanded Abstracts, 742–747.

Liu, C., L. C. Shen, and Y. C. Zhang, 1995, Monitoring saltwater injection using conductivity images obtained by electromagnetic cross-hole measurements: Radio Science, **30**, 1405–1415.

Liu, J., A. Abubakar, T. M. Habashy, D. L. Alumbaugh, N. E., and G. Gao, 2008, Nonlinear inversion approaches for cross-well electromagnetic data collected in cased wells: 78th Annual International Meeting, SEG, Expanded Abstracts, 304–308.

Marsala, A. F., S. B. Al-Ruwaili, M. M. Shouxiang, Z. A. Al-Ali, M. H. Al-Buali, J.-M. Donadille, S. Crary, and M. Wilt, 2008, Crosswell electromagnetic tomography: from resistivity mapping to interwell fluid distribution: International Petroleum Technology Conference, doi:10.2523/IPTC–12229–MS.

Marsala, A. F., S. Lyngra, M. Safdar, and M. Zhang, P. Wilt, 2015, Crosswell electromagnetic induction between two widely spaced horizontal wells: Coiled-tubing conveyed data collection and 3d inversion from a carbonate reservoir in saudi arabia: 85th Annual International Meeting, SEG, Expanded Abstracts, 2848–2852.

Menke, W., 2018, Geophysical data analysis: Discrete inverse theory (fouth edition): Academic Press Inc.

Newman, G. A., and D. L. Alumbaugh, 2002, Three-dimensional induction logging prob-

lems, Part 2: A finite-difference solution: Geophysics, **67**, 484–491.

Newman, W. I., 2016, Mathematical methods for geophysics and space physics: Princeton University Press.

Okwen, R., S. Frailey, and S. Dastgheib, 2017, Brine extraction and treatment strategies to enhance pressure management and control of CO2 plumes in deep geologic formations: Technical Report DOE-UOFI-FE0026136, USDOE Office of Fossil Energy (FE), United States.

Pair, J. D., 2017, The tuscaloosa marine shale: Geologic history, depositional analysis, and exploration potential: PhD thesis, Stephen F. Austin State University.

Phillips, S. L., A. Igbene, J. A. Fair, H. Ozbek, and M. Tavana, 1981, A technical databook for geothermal energy utilization: Technical Report LBL-12810, Lawrence Berkeley National Laboratory.

Schlumberger, 2009, Schlumberger log interpretation charts, 2009 edition: http://pages.geo.wvu.edu/~tcarr/pttc/schlumberger_chartbook.pdf, accessed 15 April 2019.

Shen, J.-S., W.-B. Sun, W.-J. Zhao, and W.-C. Zeng, 2008, A 2.5D cross-hole electromagnetic modelling and inversion method and its application to survey data from the Gudao oil field, East China: Journal of Geophysics and Engineering, **5**, 401–411.

Siirila-Woodburn, E. R., A. Cihan, and J. T. Birkholzer, 2017, A risk map methodology to assess the spatial and temporal distribution of leakage into groundwater from geologic carbon storage: International Journal of Greenhouse Gas Control, **59**, 99–109.

Spies, B. R., 1992, Survey design considerations for cross-well electromagnetics: 62nd Annual International Meeting, SEG, Expanded Abstracts, 498–501.

Spies, B. R., and T. M. Habashy, 1995, Sensitivity analysis of crosswell electromagnetics:

Geophysics, **60**, 834–845.

Spivey, J. P., W. D. McCain, and R. North, 2004, Estimating density, formation volume factor, compressibility, methane solubility, and viscosity for oilfield brines at temperatures from 0 to 275° C, pressures to 200 MPa, and salinities to 5.7 mole/kg: Journal of Canadian Petroleum Technology, **43**, 52–61.

Tripp, A. C., and G. W. Hohmann, 1993, Three-dimensional electromagnetic cross-well inversion: IEEE Transactions on Geoscience and Remote Sensing, **31**, 121–126.

U.S. Department of Energy, 2016, Energy department selects projects to demonstrate feasibility of producing usable water from CO2 storage sites: https://www.energy.gov/fe/articles/energy-department-selects-projects-demonstrate-feasibility-producing-usable-water-co2, accessed 20 May 2020.

van der Horst, M., V. Druskin, and L. Knizhnerman, 1999, Modeling induction logs in 3-D geometries, *in* Three-Dimensional Electromagnetics: SEG.

Wilkinson, P. B., 2005, Cross-borehole electromagnetic tomography - scoping study and literature review: Technical Report IR/05/146, British Geological Survey, Keyworth, Nottingham.

Wilt, M. J., D. L. Alumbaugh, H. F. Morrison, A. Becker, K. H. Lee, and M. Deszcz-Pan, 1995a, Crosswell electromagnetic tomography: System design considerations and field results: Geophysics, **60**, 871–885.

Wilt, M. J., J. M. Donadille, S. AlRuwaili, S. M. Ma, and A. Marsala, 2008, Crosswell electromagnetic tomography in Saudi Arabia - from field surveys to resistivity mapping: 70th EAGE Conference and Exhibition.

Wilt, M. J., and M. Morea, 2004, 3D waterflood monitoring at Lost Hills with crosshole EM: The Leading Edge, **23**, 489–493.

Wilt, M. J., H. F. Morison, A. Becker, H. W. Tseng, K. H. Lee, C. Torres-Verdin, and D. L. Alumbaugh, 1995b, Croshole electromagnetic tomography: A new technology for oil field characterization: The Leading Edge, **14**, 173–177.

Winsauer, W. O., H. M. Shearin, P. H. Masson, and M. Williams, 2017, Resistivity of brine-saturated sands in relation to pore geometry: AAPG Bulletin, **36**, 253–277.

Wu, X., and T. M. Habashy, 1994, Influence of steel casings on electromagnetic signals: Geophysics, **59**, 378–390.

Zhang, J., and C. R. Liu, 2000, Two-dimensional conductivity image from the data measured by electromagnetic crosswell tools: Subsurface Sensing Technologies and Applications II, International Society for Optics and Photonics, SPIE, 180–189.

Zhang, P., W. Abdallah, M. Ramadhan, A. Marsala, S. Saif, S. Lyngra, and S. Ma, 2017, Crosswell electromagnetic survey: An effective approach for reservoir-scale saturation mapping: 87th Annual International Meeting, SEG, Expanded Abstracts, 1054–1058.

Zhang, Y., C. Liu, and L. C. Shen, 1996, A TLM model of a borehole electromagnetic sensing system: Journal of Applied Geophysics, **36**, 77–88.

Zhdanov, M. S., and K. Yoshioka, 2003, Three-dimensional cross-well electromagnetic tomography: 73rd Annual International Meeting, SEG, Expanded Abstracts, 526–529.

LIST OF TABLES

VMD and VED data sets. RMS errors are based on a real-and-imaginary field representation (as opposed to amplitudes and phases). The VMD data set comprises 1323 complex magnetic-field data points, whereas the VED set has 63 electric fields; VMD+VED is the merged set.

LIST OF FIGURES

7   Major geological units at the BEST injection site. The considered injection zone is the Lower Tuscaloosa Massive Sand (1487 m to 1536 m). Also shown are resistivity and porosity profiles measured at well TIW-2.

8   Flow simulation of an 18-months long freshwater injection into the well TIW-2, where freshwater is electrically resistive with respect to the native (highly saline) brine. Salinity varies as dimensionless NaCl mass fraction. The upper horizontal surface sketches the survey area (as shown by Figure 1) and the vertical layered plane sketches the underlying one-dimensional permeability model. Pressure management tasks consider a hypothetical fault as potential hazard. Note that the upper plume region (above z=1500 m) at TIW-2 remains electrically conductive due to a thin impermeable layer.

9   Horizontal sensitivity maps for the VMD and VED crosswell configurations employed at the BEST site. (a) VMD setup with two transmitter-receiver arrays; the first transmits at TIW-2 and receives at TEMW-A; the second transmits at TIW-1 and receives at TIW-2 and TEMW-A. (b) VMD amplitude sensitivity (D_{amp}^{rel}) map. (c) VMD phase sensitivity (D_{pha}^{rel}) map. (d) VED setup, where the arrow points from the transmitter array in the injection well (TIW-2) to the receiver array in TIW-1. (e) VED amplitude sensitivity (D_{amp}^{rel}) map. (f) VED phase sensitivity (D_{pha}^{rel}) map. Sensitivities are calculated using equation 9, where D_{amp}^{rel} and D_{pha}^{rel} involve field-amplitude and phase (in degrees) data, respectively.

10   Synthetic crosswell EM inversions for the BEST site's freshwater plume model. (a) True plume model after 365 days of injection at the BEST site. (b) Inversion of VMD data (layout shown in Figure 9a). (c) Inversion of VED data (layout shown in Figure 9c). (d) Joint inversion of VMD and VED components.

11   Data fits exemplified for a selected VMD (a and b) and VED (c and d) subset.

Fitted data are complex and are post-converted to amplitudes and phases.

12   Variable lower parameter bounds over the inversion domain of the BEST study. (a) True plume model after 365 days of injection. (b) Ellipsoidal volume with lower parameter bounds that increase linearly away from the center. Semiaxes are $(dx, dy, dz)=$(500,500,120) m. (c) Profile along the line $y=0$ m which traverses the plume center and exemplifies the variable lower bounds (solid lines) in comparison with the actual conductivities (gray dashed). Also shown is the level for the constant lower bound (dotted line) used for the first trial VED data inversion (image in Figure 10c).

13   Inversion of VED component for the BEST site's freshwater plume model at $t=$180 days and $t=$365 days. (a) Actual plume at 180 days. (b) Inversion for plume at 180 days. (c) Actual plume at 365 days. (d) Inversion for plume at 365 days. Both inversions employ variable lower parameter bounds (as illustrated in Figure 12).
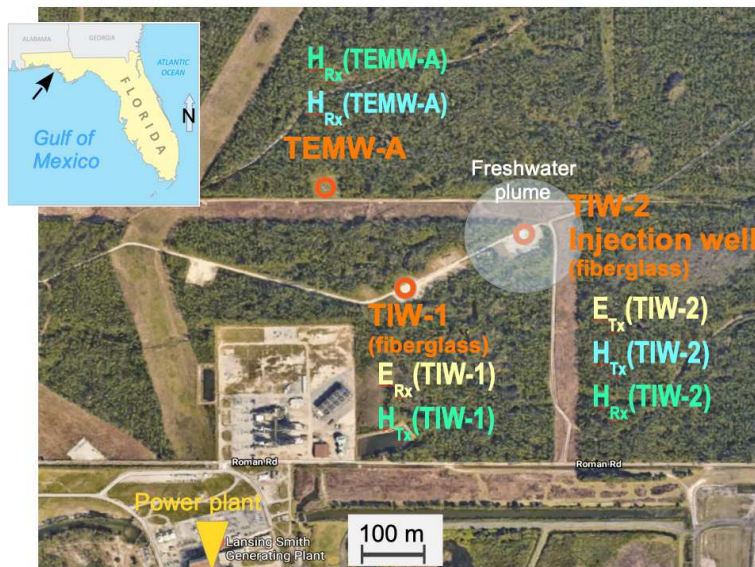
Figure 1: Site map of the BEST site near Lansing Smith Generating Plant (Southport, near Panama City, Florida) with injection (TIW-2) and monitoring/extraction wells (TIW-1 and TEMW-A).

_
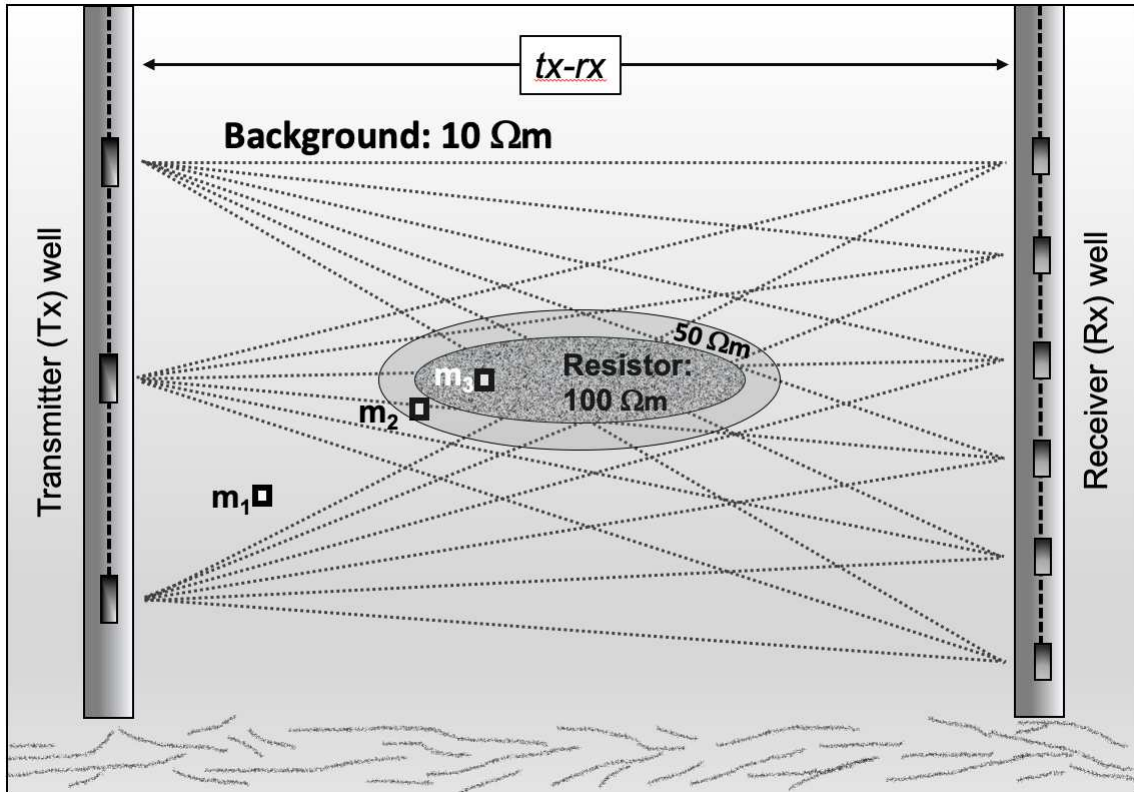
Figure 2: Schematic of a crosswell EM system.

–

a)

$$f(x)=\frac{1}{1+e^{x_c-x}}$$

$x_c=0$

f(x)

x

b)

Model "standard deviation", $\delta(m_i)$

$\delta^{max}=10$

$\delta+(m_i)$ ——————
$\delta-(m_i)$ - - - - - ·

$\delta^{min}=1$

σ^{lim}

Model cell value, $m_i=\sigma_i$ (S/m)
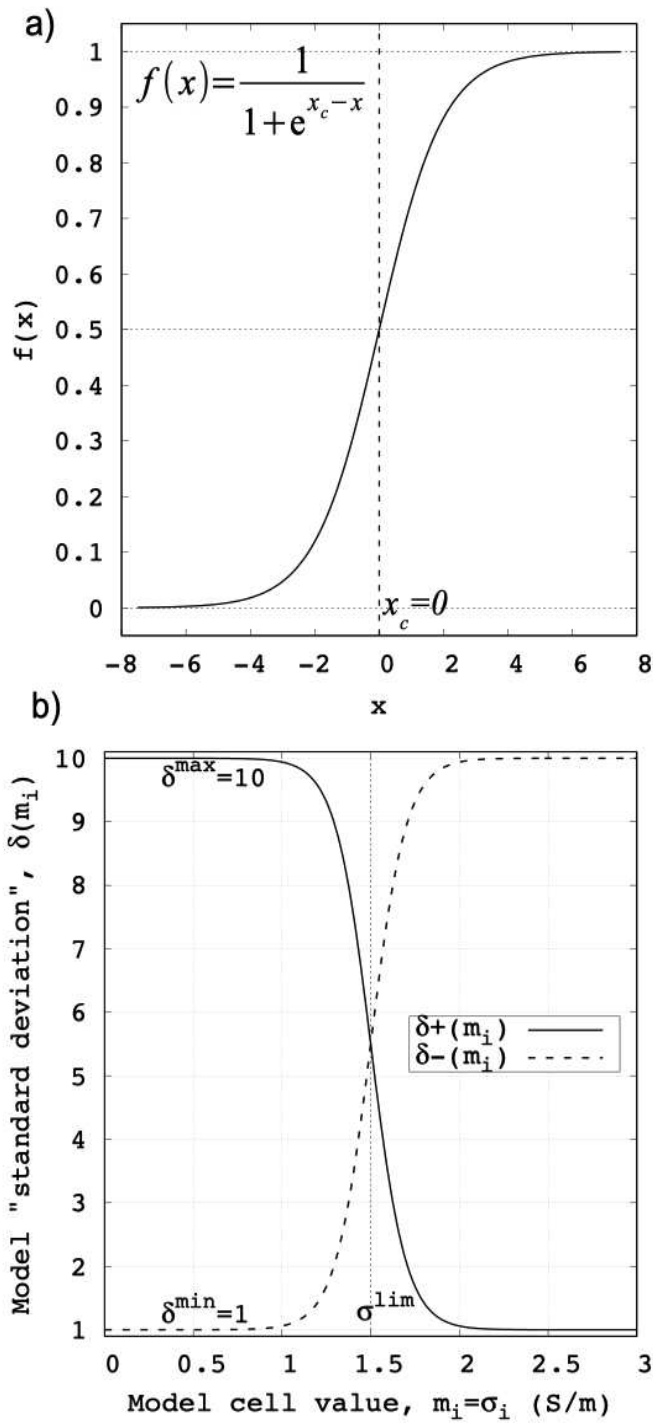
Figure 3: (a) Example for a logistic function, which belongs to the class of sigmoidal functions. (b) Example for a logistic function which makes the weighting $(\frac{1}{\delta})$ of RMS error contributions model dependent. Equations 4 and 5 produce the descending (δ^+) and ascending (δ^-) curves. The steepness is controlled by the scaling factor $s > 0$ (here $s = 0.1$), which has units of the model property m.
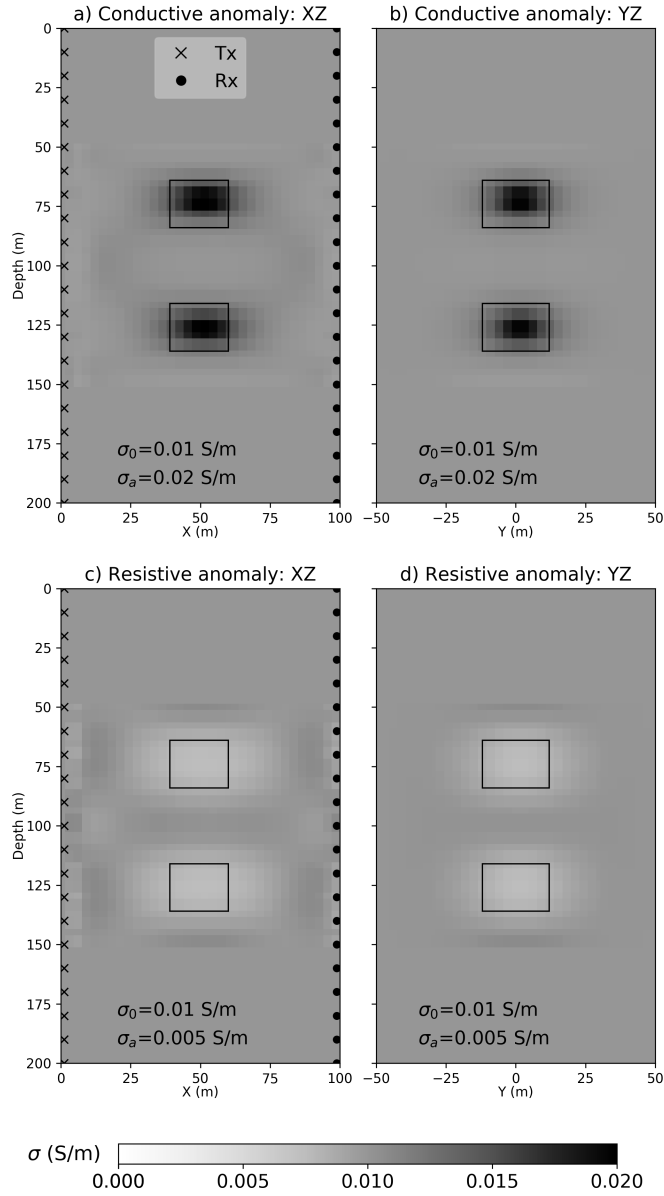
Figure 4: Synthetic 3D crosswell inversion experiment modeled after the 2D VMD configuration of Alumbaugh and Morrison (1995b). Final images obtained after 156 NLCG inversion iterations are shown for a conductive anomaly (a and b) and for a resistive anomaly (c and d).
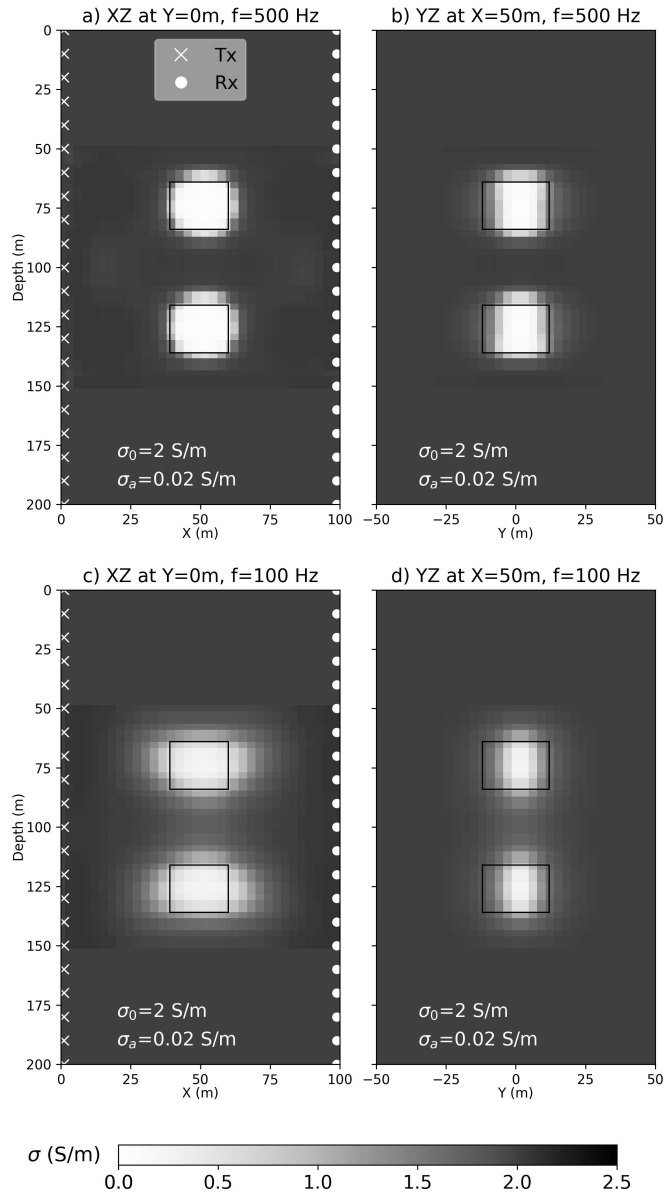
Figure 5: Synthetic 3D crosswell inversion experiment modeled after the 2D VMD configuration of Alumbaugh and Morrison (1995b). Background and anomalous conductivity approximate conditions at the BEST site. Final images obtained after 156 NLCG inversion iterations are shown for the source frequency 500 Hz (a and b) and for the source frequency 100 Hz (c and d).
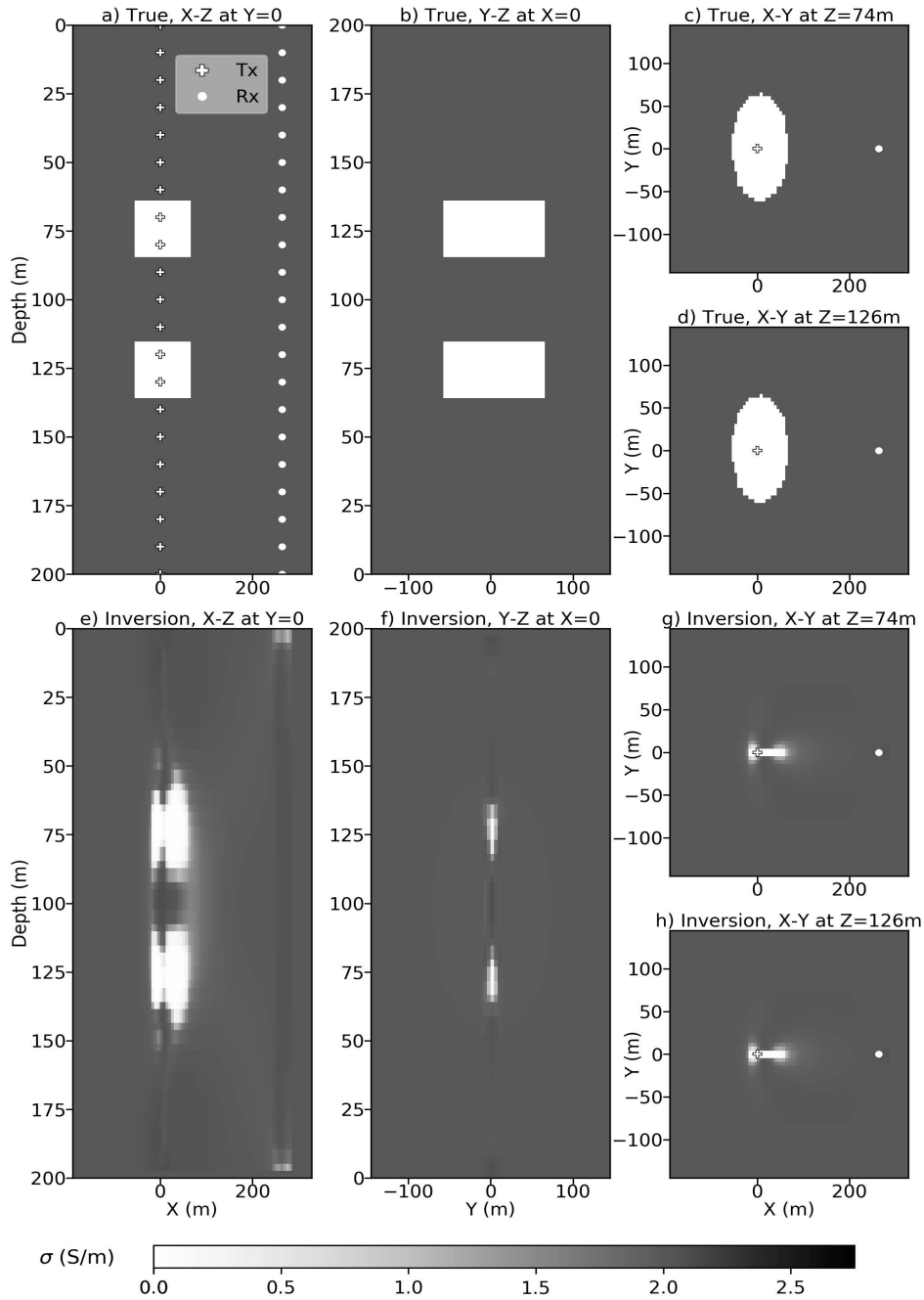
Figure 6: Synthetic 3D VMD crosswell inversion experiment implementing survey conditions at the BEST site. Two cylindrically shaped resistors (true model shown by a-d) are symmetric about the injection well (at $x=0$), which coincides with the transmitter array. The receiver array is at a distance of 264 m. Final images (e–h) obtained after 156 NLCG inversion iterations involve the source frequency 100 Hz.

–
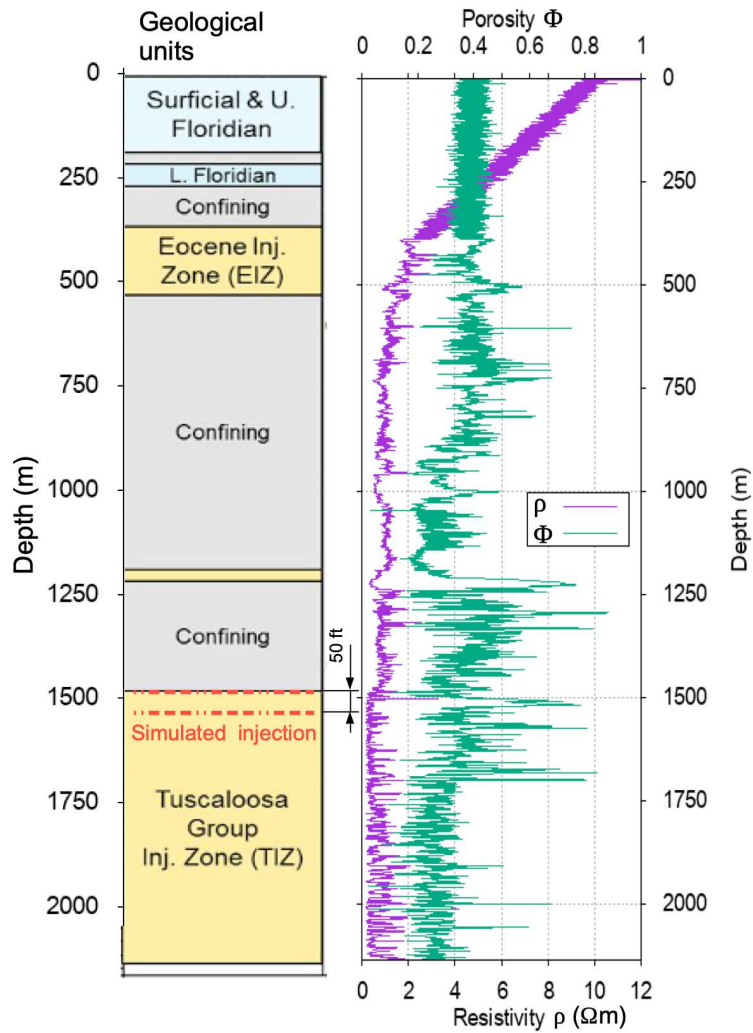
Figure 7: Major geological units at the BEST injection site. The considered injection zone is the Lower Tuscaloosa Massive Sand (1487 m to 1536 m). Also shown are resistivity and porosity profiles measured at well TIW-2.

–
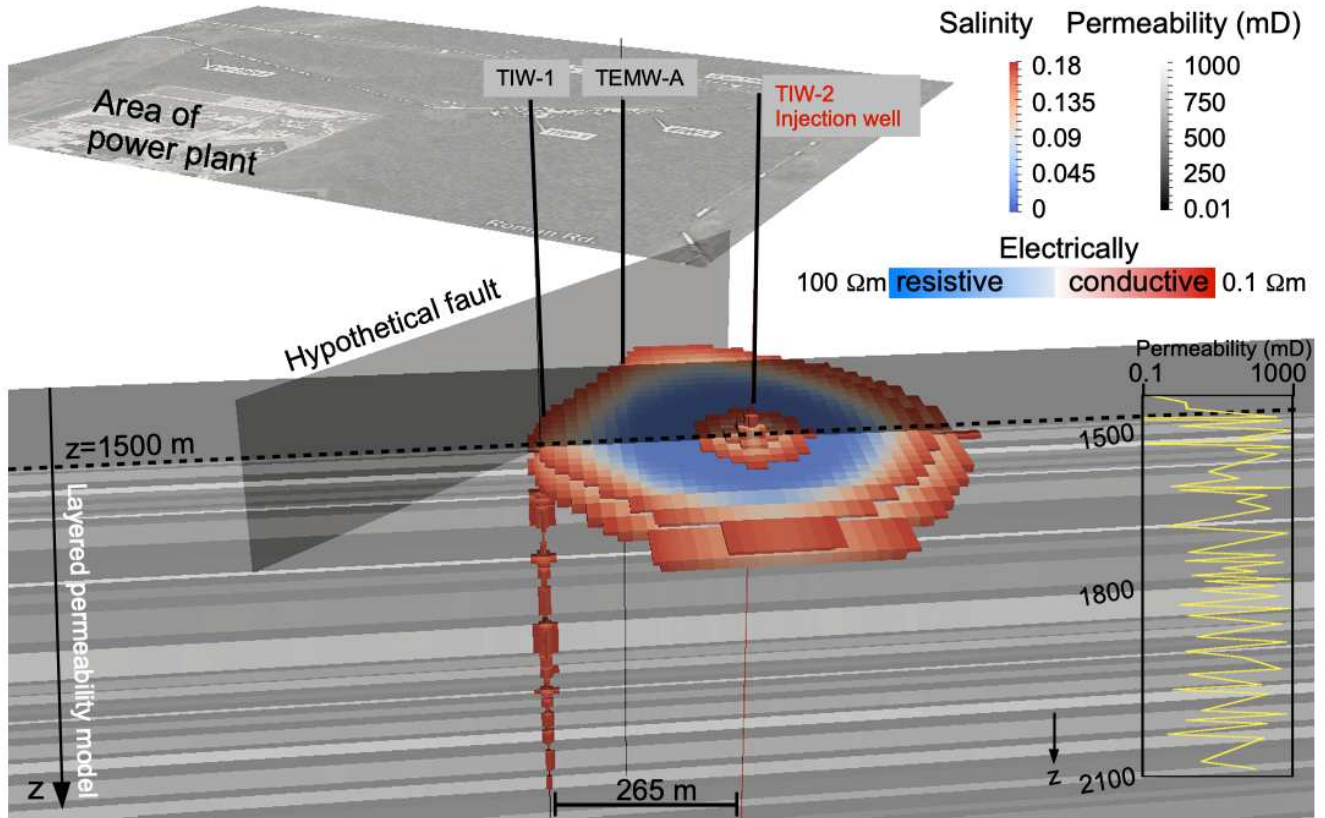
Figure 8: Flow simulation of an 18-months long freshwater injection into the well TIW-2, where freshwater is electrically resistive with respect to the native (highly saline) brine. Salinity varies as dimensionless NaCl mass fraction. The upper horizontal surface sketches the survey area (as shown by Figure 1) and the vertical layered plane sketches the underlying one-dimensional permeability model. Pressure management tasks consider a hypothetical fault as potential hazard. Note that the upper plume region (above z=1500 m) at TIW-2 remains electrically conductive due to a thin impermeable layer.

_
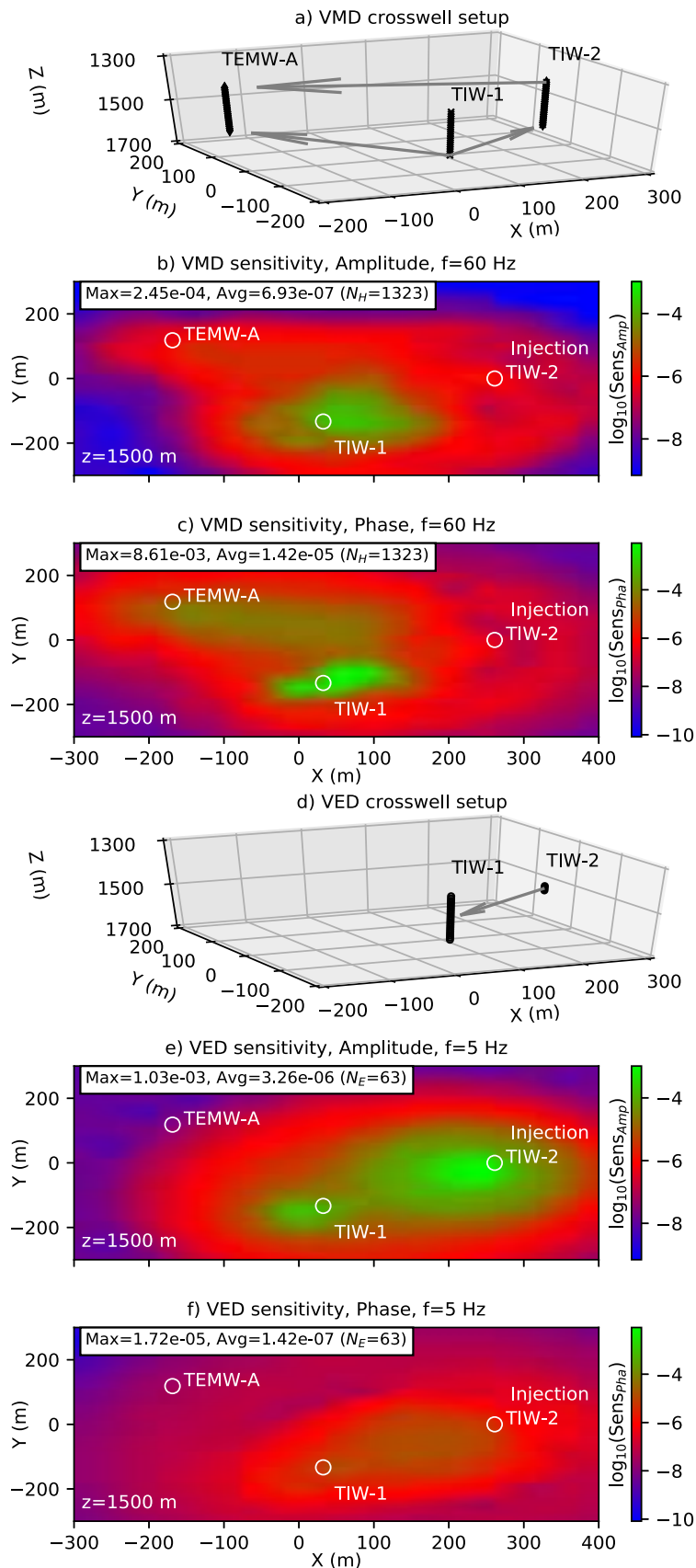
Figure 9: Horizontal sensitivity maps for the VMD and VED crosswell configurations em-
ployed at the BEST site. (a) VMD setup with two transmitter-receiver arrays; the first

54
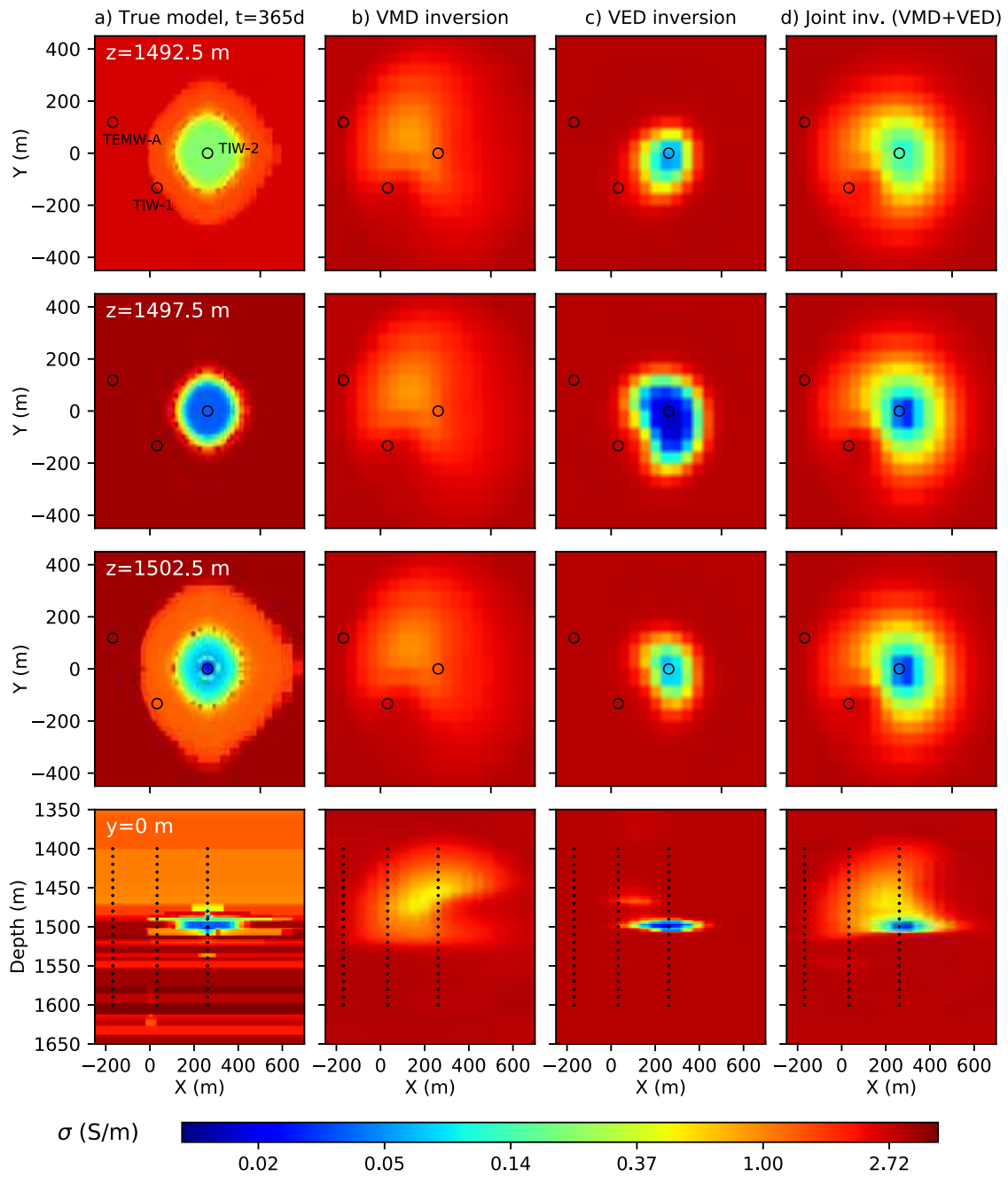
Figure 10: Synthetic crosswell EM inversions for the BEST site's freshwater plume model.

(a) True plume model after 365 days of injection at the BEST site. (b) Inversion of VMD data (layout shown in Figure 9a). (c) Inversion of VED data (layout shown in Figure 9c). (d) Joint inversion of VMD and VED components.
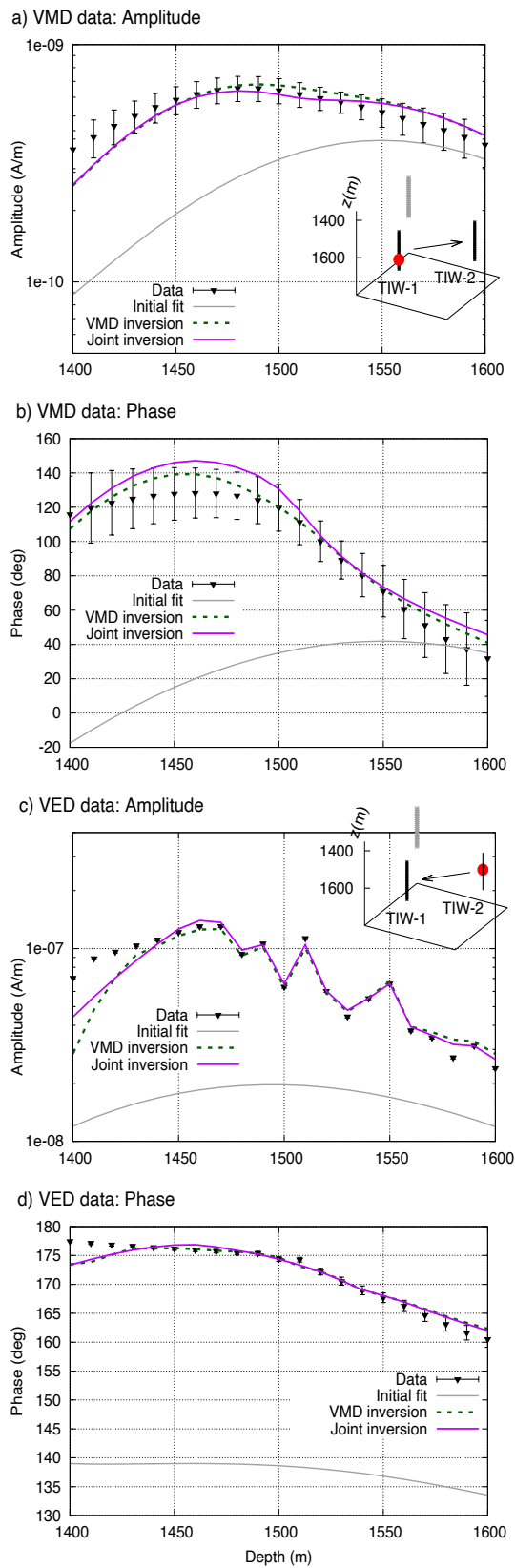
Figure 11: Data fits exemplified for a selected VMD (a and b) and VED (c and d) subset.

Fitted data are complex and are post-converted to amplitudes and phases.
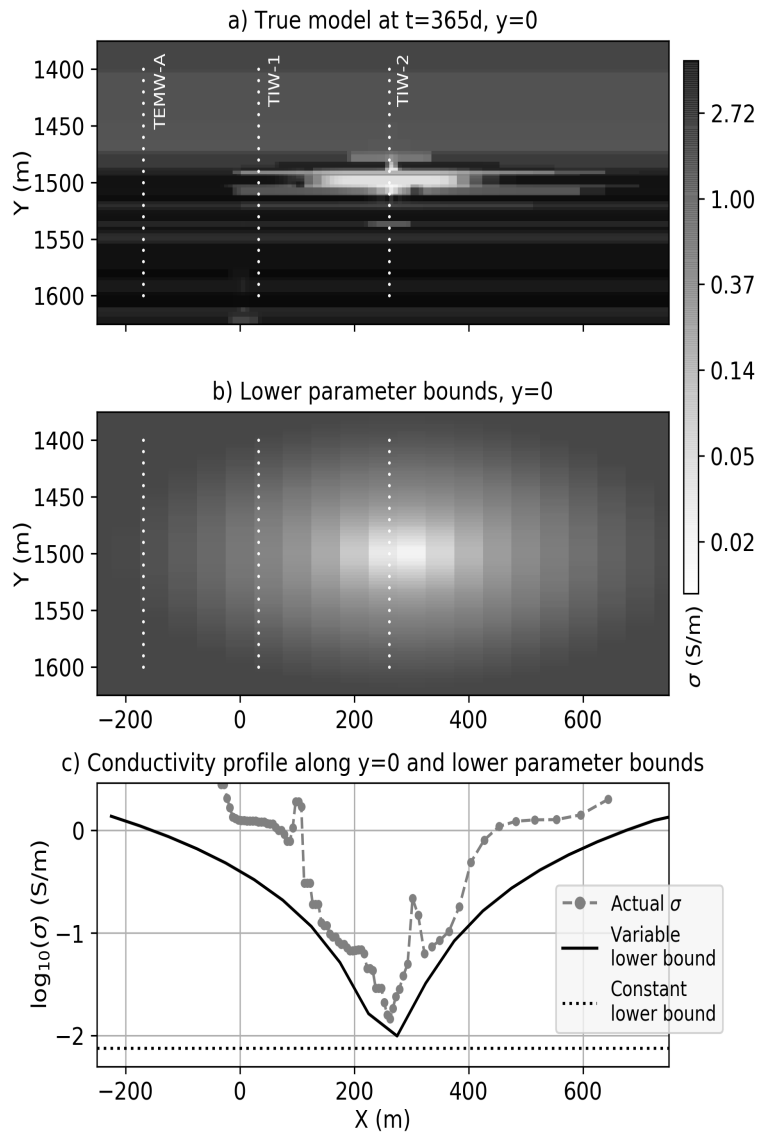
Figure 12: Variable lower parameter bounds over the inversion domain of the BEST study. (a) True plume model after 365 days of injection. (b) Ellipsoidal volume with lower parameter bounds that increase linearly away from the center. Semiaxes are $(dx,dy,dz)=(500,500,120)$ m. (c) Profile along the line $y=0$ m which traverses the plume center and exemplifies the variable lower bounds (solid lines) in comparison with the actual conductivities (gray dashed). Also shown is the level for the constant lower bound (dotted line) used for the first trial VED data inversion (image in Figure 10c).

—
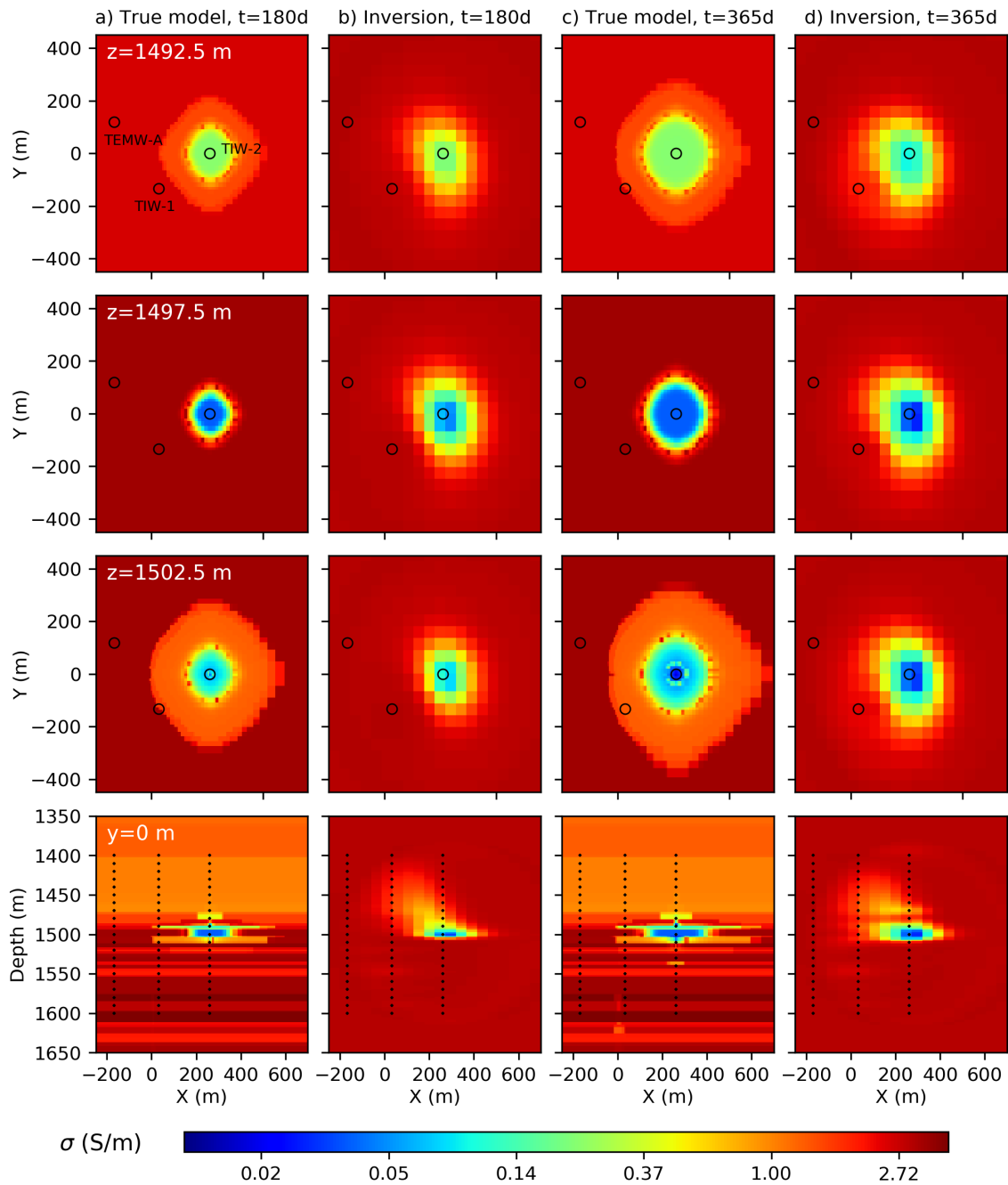
Figure 13: Inversion of VED component for the BEST site's freshwater plume model at t=180 days and t=365 days. (a) Actual plume at 180 days. (b) Inversion for plume at 180 days. (c) Actual plume at 365 days. (d) Inversion for plume at 365 days. Both inversions employ variable lower parameter bounds (as illustrated in Figure 12).

Inversion No.	1	2	3	4	5
Figure No.	4a and 4b	4c and 4d	5a and 4b	5c and 5d	6e − 6h
Source frequency	31 kHz	31 kHz	500 Hz	100 Hz	100 Hz
Background σ_0 ($\frac{S}{m}$)	0.01	0.01	2	2	2
Anomaly σ_a ($\frac{S}{m}$)	0.02	0.005	0.02	0.02	0.02
ε (%)	30.89	19.49	46.69	37.19	5.65
ε^{log} (%)	32.86	20.71	27.68	17.78	3.10
$\delta^{\pm}$	δ^-	δ^+	δ^+	δ^+	δ^+
σ^{lim} ($\frac{S}{m}$)	0.012	0.008	1.0	1.0	1.0
ε_δ (%)	67.08	25.09	56.28	45.08	6.54
ε_δ^{log} (%)	63.71	28.17	51.43	39.50	4.57
$[a,b]$ ($\frac{S}{m}$)	[0.01,10]	[0,0.01]	[0,2]	[0,2]	[0,2]
Δ^{lim} (%)	20	-20	-30	-30	-30
S (%)	82.14	47.86	87.14	75.36	10.61

Table 1: Image-reproduction quantifiers calculated from a series of five inversions of VMD data. Each inversion's two-body target anomaly is characterized by the true model's background (σ_0) and the anomalous conductivity (σ_a). Figure numbers refer to the resulting images, so each table column represents a separate inversion realization, without relating to other inversions. Within each column, three types of errors are (1) the difference measures ε and ε^{log}, equations 2 and 3, (2) their weighted counterparts ε_δ and ε_δ^{log}, with weights given by equations 4 and 5 (using $\delta^{min} = 1$, $\delta^{max} = 10$, $s = 10^{-4}$), and (3) the semblance measure S, equation 8. All RMS (ε) errors are calculated from the inversion's initial (starting) and final model, where only the corresponding relative %-change is shown. The parameters $\delta^{\pm}$ (type of weighting function) and σ^{lim} pertain to ε_δ and ε_δ^{log}. Further given are the semblance parameters $[a, b]$ and Δ^{lim}.

Inversion No.	Fig. No.	Data type	Injection period (d)	ε (%)	ε^{log} (%)	ε_δ (%)	ε_δ^{log} (%)	ε_{ab} (%)	ε_{ab}^{log} (%)	S (%)
1	10b	VMD	365	3.21	3.27	4.66	5.75	5.21	4.72	13.00
2	10c	VED	365	0.63	1.00	0.87	1.57	0.94	1.55	27.60
3	10d	VMD+VED	365	2.23	2.70	3.24	4.24	3.64	4.14	61.00
4	13b	VED	180	1.33	1.87	1.82	2.68	1.88	2.64	38.10
5	13d	VED	365	1.31	1.84	1.80	2.64	2.06	2.73	46.40

Table 2: Model misfit quantifiers calculated from a series of trial inversions for a freshwater plume simulated for the conditions at the BEST site. Inverted are crosswell data as simulated from the VMD and VED configurations in Figures 9a and 9c. All inversions use a homogeneous full-space ($\sigma=3\ \frac{S}{m}$) as initial model guess. Errors are given as a percentage decrease with respect to the initial model. RMS measures are ε, ε^{log} (equations 2–3), their weighted versions (ε_δ, ε_δ^{log}, where $\sigma^{lim}=2.64$), and the semblance S, equation 8. RMS terms ε_{ab} and ε_{ab}^{log} only comprise image grid elements i where the corresponding reference $\tilde{m}_i \in [a,b]$. Semblance parameters are $[a,b]=[0,1.11]$ (in $\frac{S}{m}$), and $\Delta^{lim}=$-12 % for all instances.

Data type	Complex data points	Inversion No.	Initial[1]	Final[1]	improve-ment (%)[1]	Initial[t]	Final[t]	improve-ment (%)[t]
VMD	1323	1	3.35	0.63	81.1	3.64	1.61	55.7
VMD	1323	3 (joint)	3.35	0.87	74.1	3.64	1.68	54.0
VED	63	2	28.50	6.35	77.7	22.55	4.60	79.6
VED	63	3 (joint)	28.50	5.59	80.4	22.55	4.45	80.3
VMD+ VED	1386	1+2	-	-	-	5.98	1.85	69.0
VMD+ VED	1386	3 (joint)	-	-	-	5.98	1.89	68.4

Table 3: Data RMS misfit errors pertaining to Inversion No. 1 (VMD), 2 (VED), and 3 (joint) (refer to Table 2). Initial and final RMS errors use equation 2, where superscript "1" refers to the selected example subset of Figure 11, and superscript "t" refers to the total VMD and VED data sets. RMS errors are based on a real-and-imaginary field representation (as opposed to amplitudes and phases). The VMD data set comprises 1323 complex magnetic-field data points, whereas the VED set has 63 electric fields; VMD+VED is the merged set.